JGR Solid Earth

RESEARCH ARTICLE
10.1029/2020JB020405

Key Points:
- We reproduce slow-slip events in two different geomaterials following frictional theory
- Slip velocity function and stress drop are controlled by micromechanical deformation
- Slip velocity function contains the dynamical information to characterize stress drop

Correspondence to:
M. M. Scuderi,
marco.scuderi@uniroma1.it

Citation:
Scuderi, M. M., Tinti, E., Cocco, M., & Collettini, C. (2020). The role of shear fabric in controlling breakdown processes during laboratory slow-slip events. *Journal of Geophysical Research: Solid Earth*, *125*, e2020JB020405. https://doi.org/10.1029/2020JB020405

Received 17 JUN 2020
Accepted 14 OCT 2020
Accepted article online 18 OCT 2020

Author Contributions:
Data curation: Marco M. Scuderi, Elisa Tinti, Massimo Cocco, Cristiano Collettini
Formal analysis: Marco M. Scuderi
Writing - original draft: Marco M. Scuderi, Elisa Tinti, Massimo Cocco, Cristiano Collettini

©2020. The Authors.
This is an open access article under the terms of the Creative Commons Attribution-NonCommercial License, which permits use, distribution and reproduction in any medium, provided the original work is properly cited and is not used for commercial purposes.

The Role of Shear Fabric in Controlling Breakdown Processes During Laboratory Slow-Slip Events

Marco M. Scuderi[1], **Elisa Tinti**[1,2], **Massimo Cocco**[2], **and Cristiano Collettini**[1,2]

[1]Dipartimento di Scienze della Terra, La Sapienza Università di Roma, Rome, Italy, [2]Istituto Nazionale di Geofisica e Vulcanologia (INGV), Rome, Italy

Abstract Understanding the physical mechanisms at the origin of slow-slip events has been proven a very challenging task. In particular, little is known on the role of fault heterogeneity during slow slip. In this study, we provide evidences that fault fabric controls slip velocity time histories during slow-slip events generated in the laboratory. We performed experiments using a double-direct biaxial shear apparatus and two different fault gouges, homogeneous quartz powder, and heterogeneous anhydrite/dolomite mixture. We measure details of fault slip to resolve the slip velocity function and volumetric deformation that, coupled with an analysis of the resulting microstructure, allow us to infer the mechanical processes at play. Our results show that slow-slip events can be generated for both fault gouges when $k \sim k_c$ with similar values of breakdown work. The shear fabric exerts a strong influence during the coseismic breakdown stage. In quartz, where most of the slip occurs on a very localized slipping surface, the peak slip velocity is attained near the final stage of friction breakdown and therefore a relevant amount of the mechanical work is absorbed during slip acceleration. In anhydrite/dolomite mixture, the peak slip velocity is suddenly reached after a relatively small drop in friction, accompanied by fault dilation, implying that most of the mechanical work is absorbed during slip deceleration. For anhydrite/dolomite mixture these results are likely related to heterogeneous slip distribution along the observed foliation. Taken together, these observations suggest that the mechanics of slow-slip events depends on shear zone fabric.

1. Introduction

Despite their discovery almost two decades ago (Obara, 2002; Rogers & Dragert, 2003) slow-slip events and all the transient phenomena associated with them still represent a conundrum in earthquake physics. While the growing number of geodetic and seismological observations testify that slow-slip events play a central role in the seismic moment budget during the cycle of seismogenic faults, many open questions remain on the mechanics of slow-slip events (e.g., Bürgmann, 2018; Peng & Gomberg, 2010). One of the key questions is whether slow-slip events represent a component of the composite spectrum of fault slip behavior, which also includes aseismic creep and fast "regular" earthquakes (e.g., Gomberg et al., 2016; Ide et al., 2007; Peng & Gomberg, 2010). A positive answer to this question would imply that slow-slip events can be modeled by the same constitutive laws as regular earthquakes, with the implication that we can interpret slow-slip events in terms of frictional instabilities governed by a given class of physical mechanisms. Frank and Brodsky (2019) showed that large slow-slip events are the result of a cluster of intermittent slow transients, showing a scaling of duration with moment magnitude in agreement with fast regular earthquakes. The observation that the scaling of moment magnitude with duration is similar for slow and fast earthquakes suggests that slow-slip events may share similar physical mechanisms with ordinary earthquakes, and it corroborates the assumption of the continuum spectrum of fault slip behaviors that can be described by the same class of constitutive laws (e.g., Frank & Brodsky, 2019; Gomberg et al., 2016; Hawthorne & Bartlow, 2018; Wech et al., 2010) However, the mechanics behind slow-slip events is still elusive, in particular there is not a consensus on what is the physical mechanism that limits slip velocity and controls their duration. There are a number of hypothesis on the physical mechanism(s) that can limit slip speed. Different models have been proposed relying on high fluid pressure coupled with dilation hardening (e.g., Segall et al., 2010), designed friction laws requiring an evolution from velocity weakening to velocity strengthening friction as slip accelerate (e.g., Hawthorne & Rubin, 2013; Rubin, 2011) as well as dehydration reactions that increase the internal fluid pressure of the fault zone, inducing slip acceleration by modifying the fault critical stiffness (Brantut et al., 2011). Independently of the validity of these hypotheses, these

models require the assumption of very specific boundary conditions, which should remain valid for all the different tectonic settings where slow-slip events have been observed (e.g., Peng & Gomberg, 2010; Wallace et al., 2016). Moreover, the fact that slow-slip events can nucleate on the same fault segment of regular earthquakes (e.g., Kato et al., 2012; Ruiz et al., 2014) would suggest that the same physical mechanisms can govern these fault slip behaviors.

The geological image of faults capable of hosting slow-slip events is represented by structures that are spatially heterogeneous and consist of a thick zone of deformation containing fault rocks with a strong rheological contrast (Barnes et al., 2020). In fact, from the field analysis of ancient exhumed fault zones it has been proposed that slow-slip events can arise from a mixed-mode brittle-viscous mechanism that consists in the interaction of weak networks forming a viscous matrix around stronger brittle lenses (e.g., Behr et al., 2018; Collettini et al., 2011, 2019; Fagereng & Sibson, 2010; Fagereng et al., 2014; Ujiie et al., 2018). Tremors and low-frequency earthquakes would be the result of shearing at the interface between the brittle lenses and the matrix or by direct failure within the lenses facilitated by fluid overpressure (Behr et al., 2018; Fagereng et al., 2014; Ujiie et al., 2018). Such heterogeneous fault model has been successfully used in numerical models to reproduce slow slip (e.g., Ando et al., 2010; Romanet et al., 2018; Skarbek et al., 2012).

Laboratory experiments have created the foundation for the formulation of constitutive friction laws. The Rate- and State-dependent friction (RSF) laws have been widely used to model the seismic cycle and successfully employed to simulate slow-slip events (e.g., Boatwright & Cocco, 1996; Dieterich, 1972; Romanet et al., 2018; Ruina, 1983; Skarbek et al., 2012). RSF coupled with elastic dislocation theory predicts frictional failure based on a stability condition that considers the ratio between the fault loading stiffness (k) and a critical fault rheologic stiffness (k_c) that is related to RSF constitutive parameters (Gu et al., 1984; Rice & Ruina, 1983). Following this approach, dynamic instabilities may arise at the stability boundary of $k \sim k_c$, where the elastic unloading of the surrounding medium matches the frictional weakening rate of the fault zone, allowing slip acceleration but at slow speed due to the small force imbalance. Following the conceptual framework provided by RSF theory, laboratory experiments successfully reproduced the key elements of the spectrum of fault slip behavior, by matching the fault critical rheologic stiffness (k_c) with the machine surrounding stiffness (e.g., Leeman et al., 2016; Scuderi et al., 2016; Shreedharan et al., 2019). Indeed, slow-slip events are spontaneously generated from stable sliding when $k \sim k_c$, with a transition to fast and dynamic instabilities when $k < k_c$. The stress drop and duration of the slip velocity pulse documented a continuum spectrum from slow-slip events to fast earthquakes (e.g., Leeman et al., 2016; Scuderi et al., 2016; Shreedharan et al., 2019). The analysis of the corresponding fault zone structure has shown that the onset of instabilities requires some fault fabric development (i.e., shear localization) and that the same fault structure can host both slow-slip events and fast earthquakes (Scuderi et al., 2017). However, to date, all the experiments were performed on homogenous fault gouge material (i.e., quartz) or bare rock surfaces where the deformation is highly localized, raising the question of whether slow-slip events can be generated along heterogenous experimental faults where the deformation can be distributed within the entire fault. Other laboratory experiments have also shown that slow slip may be the result of other processes such as strain weakening of the fault (e.g., Ikari et al., 2013; Ito et al., 2017), a mixed mode deformation across the brittle ductile transition (Schubnel et al., 2006), or related with high fluid pressure (French & Zhu, 2017).

In this study, following friction theory, we generated laboratory slow-slip events in both a homogeneous (localized deformation) and heterogeneous materials (distributed deformation) to study the response of different fault gouges. We investigated the role of fault fabric and strain localization on dynamic parameters (stress drop, slip velocity function, and duration) inferred during slow-slip events. In particular, we studied the temporal evolution of the weakening behavior in terms of friction, slip velocity, and volumetric deformation. Finally, we computed the mechanical work absorbed during the breakdown process and we related it to the different slip localization styles of the fault gouges. Slow-slip events emerge in the laboratory experiments under the boundary condition $k \sim k_c$ (Leeman et al., 2016; Scuderi et al., 2016) using two different fault gouge materials such as quartz and a mixture of anhydrite and dolomite. The latter fault gouge composition represents an analog of the Triassic Evaporites, which is the formation where seismicity in the Apennines, Italy, occurs (Crescentini, 1999; De Paola et al., 2008; Gualandi et al., 2017; Latorre et al., 2016; Miller et al., 2004; Mirabella et al., 2008). We measure the RSF constitutive parameters to achieve the boundary conditions to reproduce slow-slip events for both fault gouges. Following an integrated analysis of the

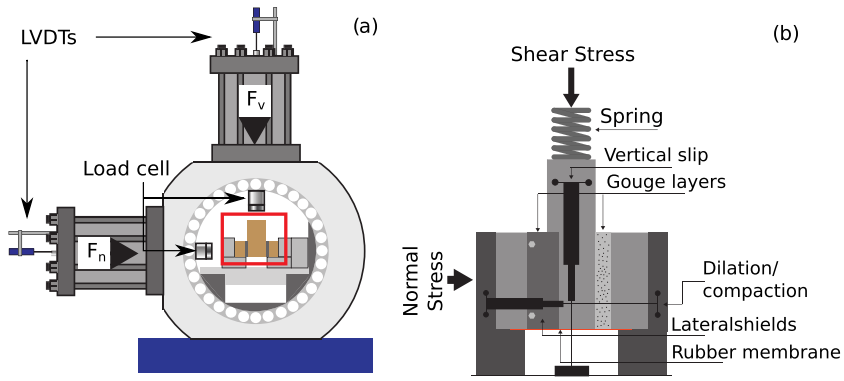

Figure 1. Schematic representation of the experimental apparatus and shear configuration. (a) Biaxial deformation apparatus set up in a double-direct shear configuration. Two orthogonal rams apply normal and shear stress to the sample assembly. Load cells are used to measure/control applied loads, and two LVDTs are used to measure the rams displacements. (b) Double-direct shear sample assembly equipped with two LVDTs to measure locally fault slip and layer dilation/compaction. To obtain slow-slip events, we position a spring in series with the vertical ram to decrease the stiffness of the apparatus.

mechanical data characterizing slow-slip events with microstructural observations of the resulting fault zone structure, we aim at understanding the physical processes at the origin of slow-slip events.

2. Experimental Methods

We performed laboratory experiments using a biaxial apparatus, BRAVA, (Collettini et al., 2014) configured in a double-direct shear (DDS) configuration (Figure 1). The apparatus consists in two hydraulic, fast acting, servo-controlled rams with a perpendicular geometry used to apply a horizontal and vertical force (Figure 1a). Each ram is equipped with a strain gage load cell (LEANE International model CCDG-0.1-100-SPEC) to measure the applied force with an accuracy of ±0.03 kN and a maximum force of 1.5 MN, which are regularly calibrated. Displacement transducers (LVDT, Linear Variable Displacement Transformer) are fixed between the load frame and the moving piston and are used to measure the piston movement with an accuracy of ±0.01 μm. Load point displacement measurements are corrected for the stiffness of the testing apparatus, with nominal values of 386.12 kN/mm for the vertical frame and 329.5 kN/mm for the horizontal frame. Each ram can be controlled in either load feedback mode, to maintain a constant load and measure the resulting displacement, or in displacement feedback mode, to advance the ram at a constant displacement rate. All the output signals, from the load cell and LVDTs, are recorded using a simultaneous multichannel analog to digital converter with 24 bit/channel resolution at a sampling rate of 10 kHz and then averaged for storage at rates between 1 Hz and 10 kHz.

The DDS configuration consists in three steel block assembly, composed by two side stationary block and a central forcing block, that sandwich two identical layers of simulated fault gouge (Figure 1b). The gouge layers are prepared using precise leveling jigs to achieve a uniform layer thickness of 3 mm over an area of 50×50 mm^2 to which we refer all the measurements of stress. All the experiments were performed under room temperature and 100% relative humidity (Table 1).

In these experiments, we simulate gouge layers using synthetic quartz powders and a mixture of anhydrite and dolomite 50–50 wt%. The quartz powders (Min-U-Sil 40, U.S. Silica Co.) are characterized by a mean grain size of ~10 μm and composed of 99.5% SiO_2 and traces of metal oxides, the same used in Leeman et al. (2016) and Scuderi et al. (2016). To prepare the mixture of anhydrite and dolomite (ANH/DOL), we collected samples of dolomite from outcrop in Tuscany and anhydrite from deep borehole in the Umbria-Marche Apennines (e.g., Trippetta et al., 2013). X-Ray Diffraction (XRD) analyses show that the samples are relatively pure with a mineralogical composition of >95% of dolomite and >95% of anhydrite, respectively (De Paola et al., 2008). To obtain powders, we crushed the intact rock in a disk mill and sieved to a grain size <125 μm, then we mixed the two lithologies to obtain a 50–50% mixture by weight. We choose to use this mixture since it is representative of the Triassic Evaporites (De Paola et al., 2008) that

Table 1
List of All the Experiments and Boundary Conditions

Exp N.	Material	Normal stress (MPa)	Boundary conditions	Comments
B720	Quartz	15	Stiff system	Velocity steps throughout the experiments. Velocity sequence 10-1-3-10
B721	Quartz	25	Stiff system	Velocity steps throughout the experiments. Velocity sequence 10-1-3-10
B768	Quartz	15–35	Stiff system	Slide-hold-slide
B737[a]	Quartz	15	Destiffened system $K \sim 1$	Slow-slip events
B744	Quartz	15	Destiffened system $K \sim 1$	Slow-slip events
B396	Anhydrite/dolomite	40	Stiff system	Velocity steps throughout the experiments. Velocity sequence 10-1-3-10
B766	Anhydrite/dolomite	15–35	Stiff system	Slide-hold-slide
B518[a]	Anhydrite/dolomite	35	Destiffened system $K \sim 1$	Slow-slip events
B394[a]	Anhydrite/dolomite	35	Destiffened system $K \sim 1$	Slow-slip events

[a]The samples that were used for thin sections and microstructural analysis.

represent the major seismogenic layer of Northern and Central Apennines (e.g., Miller et al., 2004; Porreca et al., 2018).

To reproduce slow-slip events in the laboratory, we first investigate the frictional properties and the constitutive parameters within the framework of the RSF law for the two fault gouges. Then, we use a spring in series with the vertical piston to reduce the stiffness and match the critical stiffness (k_c) in order to simulate slow-slip events (i.e., low stiffness experiments).

2.1. RSF Constitutive Properties and Frictional Healing

To retrieve the RSF parameters (a, b, and D_c) of the two fault gouges and to investigate the stability conditions, we have performed standard velocity step experiments (Chris Marone, 1998) (Figure 2). Each experiment begins by applying a constant normal stress of 15 or 25 MPa for quartz and 40 MPa for ANH/DOL via the horizontal ram (Table 1). Once the target normal stress is reached, the layers were allowed to compact, to ensure densification and best grain packing configuration before the onset of shearing. Shear begins by advancing the vertical ram at constant displacement rate of 10 μm/s for a displacement of ~5 mm (shear strain $\gamma \sim 2$) to reach a steady-state frictional sliding (Figure 2a). At this point a computer-controlled continuous sequence of velocity steps, for a range of shear velocities of 1, 3 to 10 μm/s, was repeated until the maximum displacement available of ~2.5 cm, resulting in shear strain $\gamma > 20$. To retrieve the RSF constitutive parameters (a-b) and D_c, we have modeled friction evolution during each velocity step using the general formulation of the RSF constitutive equations (Dieterich, 1979) (Figure 2b):

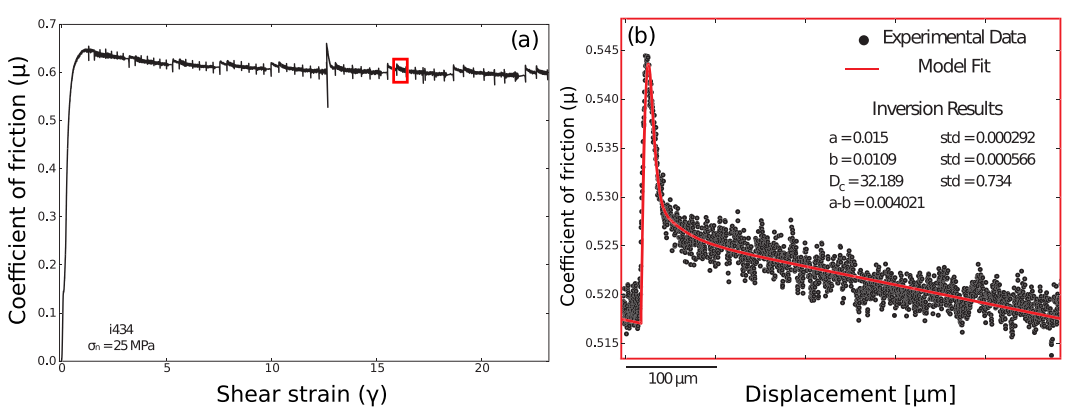

Figure 2. (a) Typical experimental curve of an experiment where velocity step tests were performed at various levels of shear strain to characterize the dependency of (a and b). (b) Zoom on a particular velocity step. We show in black the raw experimental data and in red the resulting inverted model according to the inferred constitutive parameters.

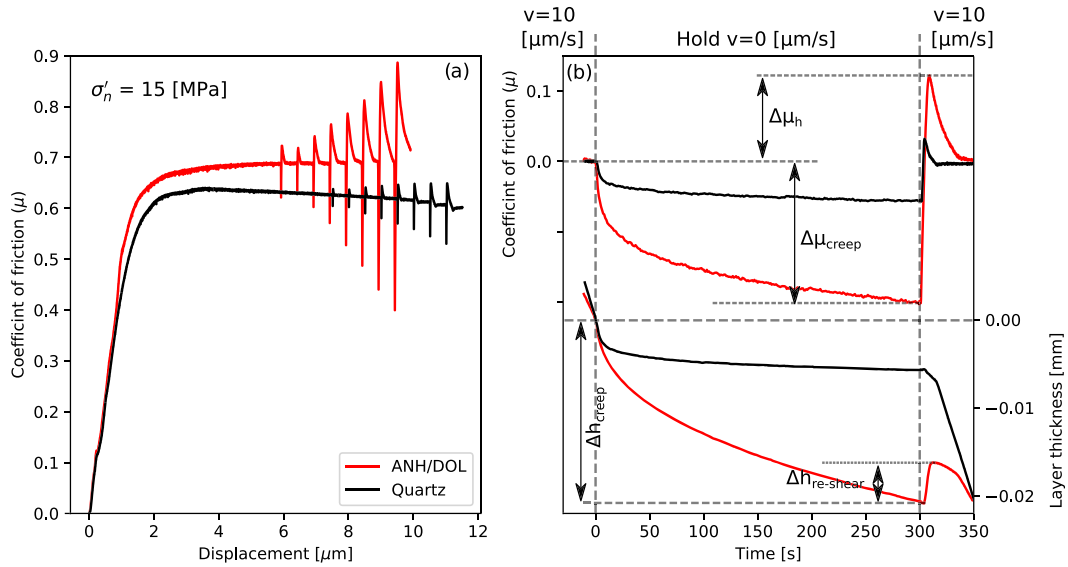

Figure 3. (a) Typical experimental curves during SHS tests for both the fault gouges used in this study showing the evolution of friction as a function of shear displacement. (b) Details of a typical SHS test (t_h = 300 s) showing the evolution of friction and layer thickness as a function of time for both fault gouges (see text for a detailed description).

$$\frac{\tau(\theta, v)}{\sigma_n} = \mu_0 + aln\left(\frac{v}{v_0}\right) + bln\left(\frac{v_0\theta}{D_c}\right) \tag{1}$$

where μ_0 represents a reference coefficient of friction at sliding velocity v_0, v is the slip rate, and a and b are the constitutive parameters. D_c is the critical slip distance, which is interpreted as the distance required to renew a population of asperity contacts, and θ is the state variable, interpreted as the average contact lifetime. In this context, the parameter (a-b) describes the stability of frictional sliding individuating two main behaviors: If (a-b) > 0, the velocity strengthening regime is indicative of aseismic creep, whereas (a-b) < 0 describes a velocity weakening behavior and it is a fundamental requisite for the nucleation of a frictional instability. We use the relation proposed by Ruina (1983) to describe the evolution of the state variable to form, together with Equation 1, the set of constitutive equations:

$$\frac{d\theta}{dt} = \frac{-v\theta}{D_c} ln\left(\frac{v\theta}{D_c}\right) \tag{2}$$

To obtain the rate-and-state constitutive parameters a, b, and D_c, we solve Equations 1 and 2 using a fifth-order Runge-Kutta numerical integration technique with adaptive step size control (Blanpied et al., 1998; Reinen & Weeks, 1993; Saffer & Marone, 2003) (Figure 2b).

To further investigate the frictional properties of both the fault gouges, slide-hold-slide (SHS) tests have been also performed following the same starting experimental procedure as described above with target normal stresses of 15 and 35 MPa (Table 1) (Figure 3). SHS tests consist in advancing the vertical ram at constant displacement rate of 10 μm/s (slide), stop shearing for a prescribed amount of time (t_h, hold time), and then resume shear at the same rate of 10 μm/s. For these tests we varied the hold time from 3 to 3,000 s with a threefold time increase. These experiments are usually performed to simulate the seismic cycle and characterize frictional restrengthening associated with interseismic stationary contact, that is, the evolution of friction due to the evolution of the state variable (e.g., Im et al., 2017; Marone & Saffer, 2015). From SHS tests it is possible to measure the frictional healing ($\Delta\mu_h$) of the fault gouge defined as the difference between the peak friction observed upon reinitiation of shear following the hold and the steady-state friction immediately prior to the hold (see Figure 3b).

Laboratory experiments usually show a log linear relation between the increase of frictional healing and the hold time, t_h (Dieterich, 1972; Scholz, 1998) even if for long hold time an exponential law has been also

observed (e.g., Nakatani, 2004). We can evaluate the rate of frictional healing (β) defined as (e.g., Marone & Saffer, 2015):

$$\beta = \frac{\Delta\mu}{\log(t_h)} \tag{3}$$

The amount of frictional healing is the direct result of contact aging during the hold time. To further characterize the friction during the hold time, we define the parameter $\Delta\mu_{\text{creep}}$ as the difference between the steady-state friction immediately prior the hold and the friction value at the end of the hold time as the creep relaxation (Figure 3b) (Carpenter et al., 2016; Ikari et al., 2016).

For each SHS we can also compute the variation in volumetric strain (i.e., layer thickness, h) to gain information on the micromechanical processes occurring during the different phases of the SHS cycle. Therefore, we measure the amount of layer compaction during the hold stage (Δh_{creep}) as the difference between the layer thickness at steady-state shearing and the instantaneous value before shear is resumed (Figure 3b). Similarly, we evaluate the amount of dilation/compaction upon resuming shear to infer the effect of particle rearrangement, $\Delta h_{\text{re-shear}}$, on fault restrengthening (e.g., Karner & Marone, 2001). The parameter $\Delta h_{\text{re-shear}}$ is defined as the difference between the peak value of thickness observed upon reinitiation of shear following the hold and the value of thickness at the end of the hold time and before shear is resumed (Figure 3b).

2.2. Slow-Slip Events Under Controlled Stiffness

In order to obtain slow-slip events in the laboratory, we follow a recently developed experimental technique, which is well described and validated in previous works (Leeman et al., 2016, 2018; Scuderi et al., 2016; Shreedharan et al., 2020; Tinti et al., 2016). In brief, by coupling elastic dislocation theory with the RSF constitutive equations for a velocity weakening fault, we can derive a criterion for fault stability described by the interaction between the surrounding stiffness, k, and a critical rheologic stiffness, k_c, defined as (e.g., Gu et al., 1984; Rice, 1983):

$$k_c = \frac{\sigma_n(b-a)}{D_c} \tag{4}$$

where k_c is derived from the analysis of the friction constitutive parameters (a-b) and D_c. This theory predicts a Hopf bifurcation when the surrounding elastic stiffness, k, is less than k_c. Within this framework, we can reproduce the full spectrum of fault slip behaviors by modulating the stiffness ratio $K = k/k_c$ to be >1 (aseismic creep), ~1 (conditionally stable), and <1 (unstable). This approach has proven successful in reproducing the full spectrum of fault slip behaviors as observed for tectonic faults (Boatwright & Cocco, 1996; Leeman et al., 2016; Scuderi et al., 2016; Tinti et al., 2016).

In this work, we first evaluate the RSF parameters of the two fault gouges and then we use an elastic element of known stiffness in series with the vertical piston to decrease the surrounding stiffness, k, to match k_c (Figure 1b). To reproduce slow-slip events, we find the appropriate boundary conditions to impose a stiffness ratio $K = k/k_c \sim 1$ and we perform all the experiments under this condition (Table 1). Due to the different fault gouge properties (frictional and rheological), the condition for $K \sim 1$ is achieved at an applied normal stress of 15 MPa for the quartz gouge and 35 MPa for the ANH/DOL gouge. To fully characterize the mechanics of slow-slip events, we equipped the DDS sample assembly with two on board displacement transducers LVDTs directly attached to the sample (Figure 1b): (1) A horizontal LVDT is used to resolve fine details of sample dilation/compaction avoiding potential artifacts from the data recorded by the remote LVDT due to the stiffness of the apparatus and (2) a vertical LVDT fixed on the moving central block and referenced at the loading frame to resolve the true fault slip of the fault and retrieve the slip velocity during the slow-slip events. Note that this represents an average slip on the entire fault surface, and we are unable to resolve the details of initiation and propagation of slip pulse. At the end of selected experiments, we also collected the resulting fault zone samples for microstructural analysis at the Scanning Electron Microscope (SEM). The procedure used to recover the samples consisted in carefully removing the applied stress field to minimize perturbations and preserve the microstructure. At this point the sample was removed from the apparatus and excess material, due to the DDS geometry, at the bottom of the assembly was cleared away. Using a thin razor blade, the sample, representing the active zone of shearing, was separated from

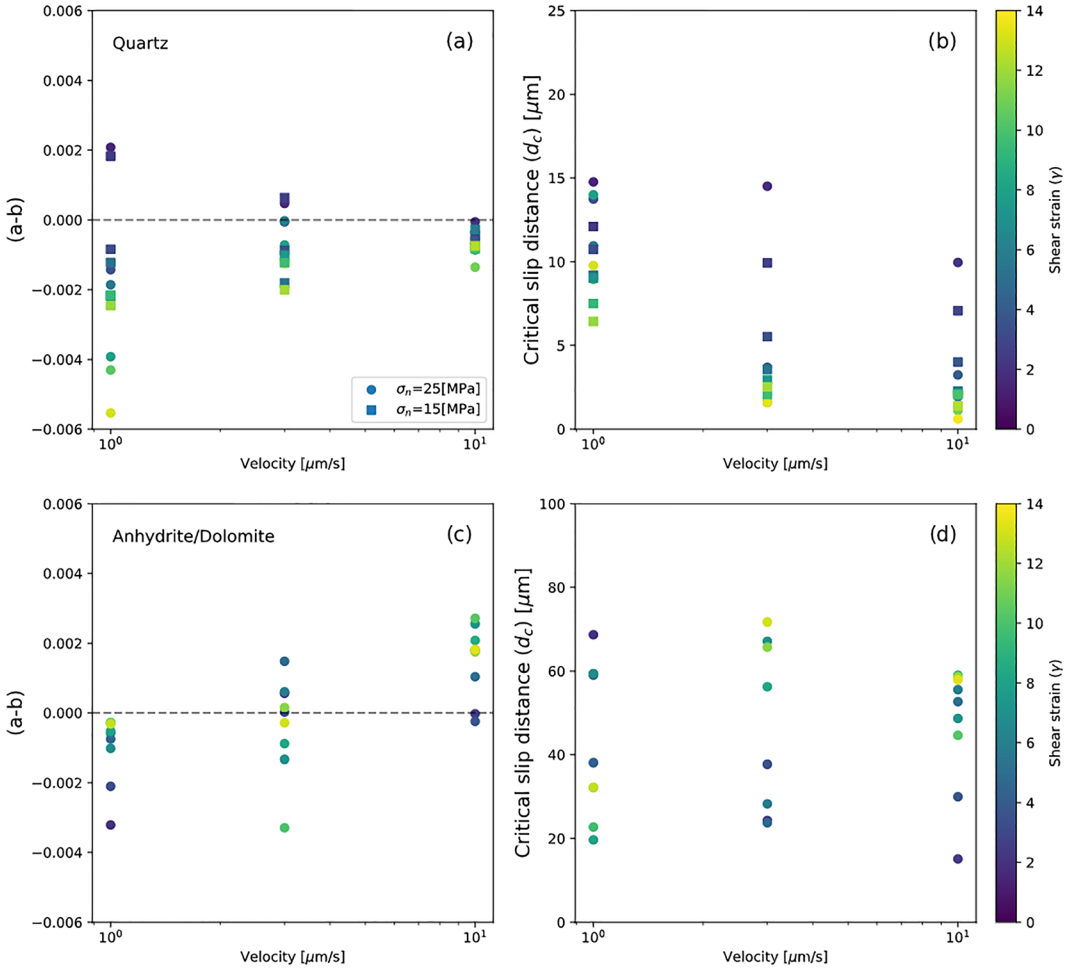

Figure 4. Top panels show RSF parameters for quartz fault gouge. (a) Evolution of the friction rate parameter (a and b) and (b) evolution of the critical slip distance as a function of shear velocity. Bottom panels show RSF parameter for ANH/DOL gouge. (c) Evolution of the rate parameter (a and b) and (d) evolution of the critical slip distance as a function of shear velocity. All the values are color coded by the correspondent shear strain at which they have been measured.

the forcing blocks and placed in a Petri dish where it was subsequently submerged in epoxy resin (Struers EpoFix Kit). The sample was then placed in a vacuum chamber and left for ~48 hr to allow the resin to penetrate within the porosity of the sample. Then, the sample was cut perpendicular to the shear direction, and small bricks were made from the central portion of the sample, avoiding the edges, to make sure we capture the active zone of deformation. Samples were then thinned using a diamond grinding wheel (the Safitec thin sectioning system) and then further polished using sand papers. To finish the sample, a polishing machine with diamond liquid (from 6 to 1 μm grain size) was used. The resulting thin section (60 μm thick) was glued to a glass dish using Logitech resin number one. We explored the microstructures at the SEM in back scattered with a beam of 20 kV, WD 10.9, and pressure 6e^{-4} Pa.

3. Results

3.1. Analysis of Fault Frictional Stability

The results obtained from velocity step experiments are summarized in Figure 4, showing the evolution of the constitutive parameters (a-b) and D_c as a function of the sliding velocity for the quartz gouge (upper panels) and for the ANH/DOL gouge (bottom panels). The friction rate parameter (a-b) has a strong dependence on both sliding velocity and accumulated shear strain. The quartz gouge shows a general velocity

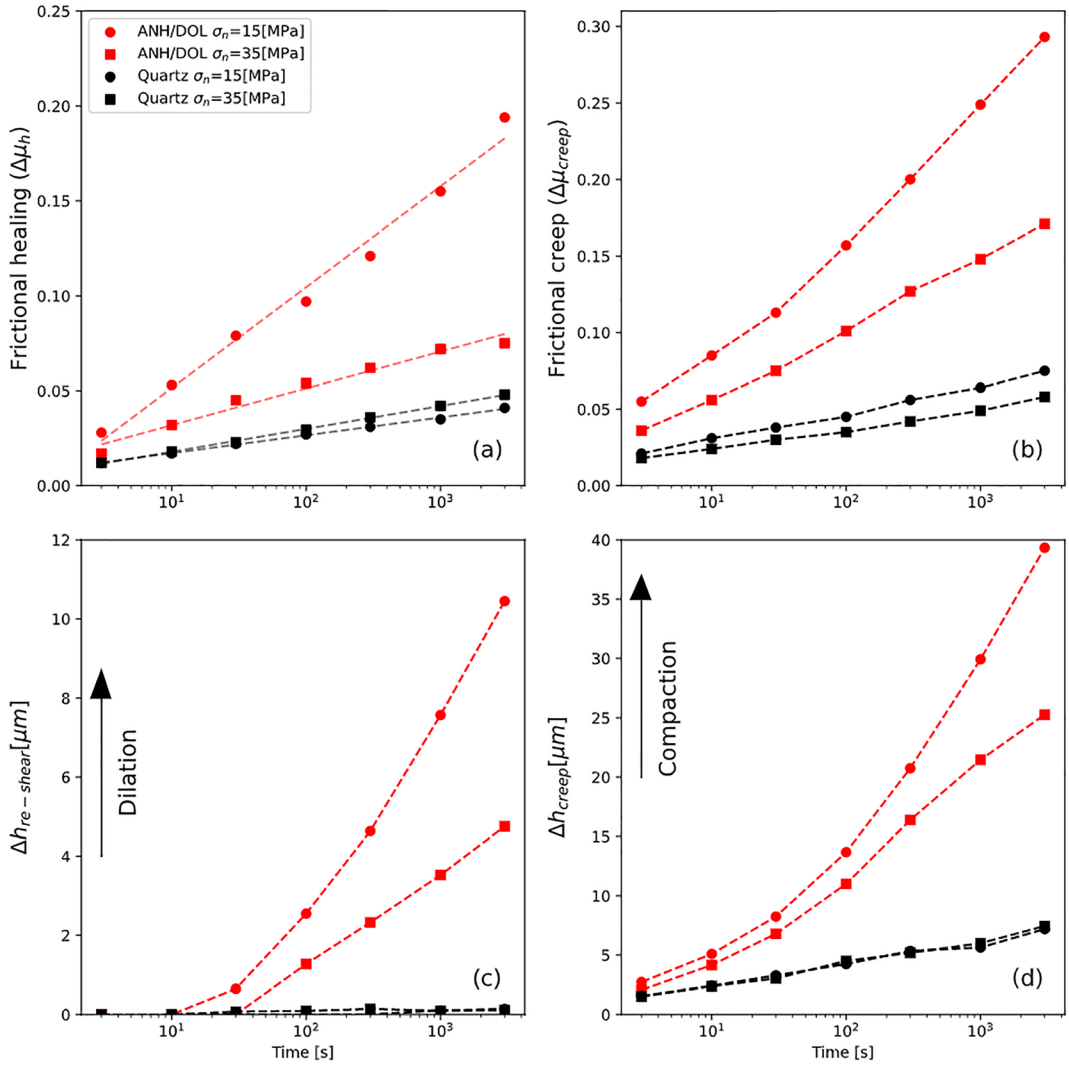

Figure 5. (a) Frictional healing, $\Delta\mu_h$, as a function of hold time for a range of normal stresses (15 and 35 MPa) and for the two investigated gouges. The dashed lines represent the best fit providing the healing rate (β). (b) Frictional creep relaxation $\Delta\mu_{\text{creep}}$ as a function of hold time. (c) Evolution of layer thickness upon fault reshear, $\Delta h_{\text{re-shear}}$. (d) Layer compaction during the hold stage, Δh_{creep}.

weakening behavior, $(a\text{-}b) < 0$, for the investigated range of shear velocity (i.e., 1, 3 to 10 μm/s), which is the condition necessary for the onset of a frictional instability (e.g., Marone, 1998; Scholz, 1998) (Figure 4a). Moreover, for the quartz gouge the $(a\text{-}b)$ parameter depends on shear strain, with the most negative values observed at higher strain (in agreement with Scuderi et al., 2017). The critical slip distance (D_c) decreases as the shear velocity is increased from values of ~10 μm at 1 μm/s, down to ~1 μm at 10 μm/s (Figure 4b). Similar to $(a\text{-}b)$, D_c also decreases with increasing shear strain, in particular during the early stages of deformation ($4 < \gamma < 6$).

For the mixture of ANH/DOL we find that the friction rate parameter $(a\text{-}b)$ evolves from a velocity weakening behavior at shear velocity of 1 μm/s to a velocity strengthening behavior when the shear rate is increased to 10 μm/s (Figure 4c). We do not observe a systematic evolution of $(a\text{-}b)$ with shear strain across the range of investigated velocities. The evolution of the critical slip distance (D_c) does not show any systematic trend, neither with shear velocity nor with accumulated shear strain, and it ranges between 80 and 20 μm (Figure 4d) that is always bigger than the values observed for quartz. For this fault gouge, persistent velocity weakening frictional behavior is observed only at shear velocity of 1 μm/s.

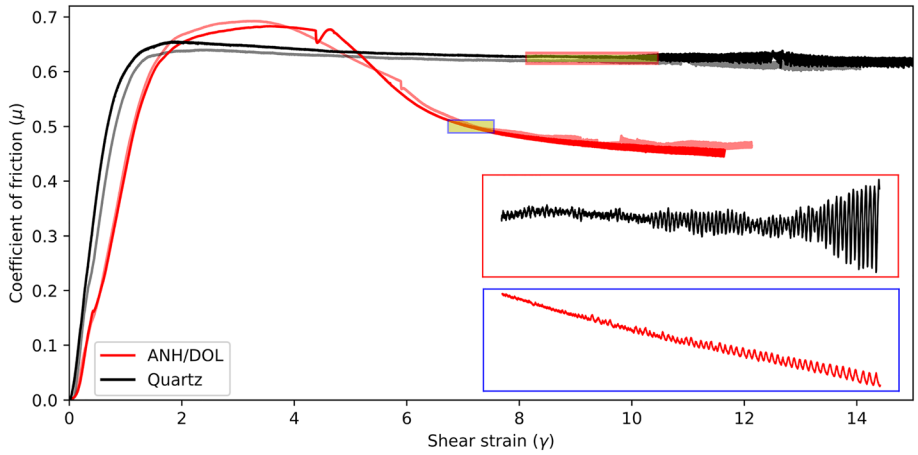

Figure 6. Typical experimental curves retrieved for experiments conducted at reduced stiffness by inserting a spring in series with the vertical piston. We report the evolution of the coefficient of friction as a function of engineering shear strain ($\gamma\gamma = \Delta h/\Delta\delta\delta$ where h is the layer thickness and δ is the shear displacement). Data for the quartz gouge are reported in black, while those for the ANH/DOL mixture in red. The two insets show the details of the spontaneous emergence of slow-slip events from steady-state shear (blue and red boxes for ANH&DOL and quartz, respectively).

The results derived from this stability analysis show that velocity weakening behavior is common for both fault gouges only at a shearing rate of 1 μm/s, resulting in a critical fault rheologic stiffness (equation 4) of 2.07e^{-4} [μm^{-1}] for quartz and 2.31e^{-5} [μm^{-1}] for ANH/DOL, suggesting us to use this shear velocity to reproduce unstable frictional behavior.

3.2. Frictional Healing

SHS tests are commonly used to mimic the seismic cycle, where the hold stage is used as a proxy for the interseismic phase and the slide stage for the coseismic phase and infer time-dependent processes that may be at the origin of subsequent failures of a seismogenic fault patch (e.g., Marone & Saffer, 2015). We evaluate the frictional healing ($\Delta\mu_h$), the healing rate ($\beta = \Delta\mu_h/\log(t_h)$), and frictional creep relaxation ($\Delta\mu_{\text{creep}}$) (see Equation 3 and Figure 3 for definitions) for the two gouges at two different values of normal stress (15 and 35 MPa) varying the hold time from 3 to 3,000 s with a threefold time increase (Figure 5). For the range of normal stresses here investigated, we find that quartz gouge has always a lower frictional healing rate ($\beta = 0.004$ [$\Delta\mu_h$/decade] at 15 MPa and $\beta = 0.005$ [$\Delta\mu_h$/decade] at 35 MPa) when compared to ANH/DOL ($\beta = 0.023$ [$\Delta\mu$/decade] at 15 MPa and $\beta = 0.008$ [$\Delta\mu$/decade] at 35 MPa) (see Figure 5a). We also find that the healing rate for quartz is roughly independent of normal stress while the ANH/DOL show a strong dependence of β on applied normal stress, decreasing as the normal stress is increased (e.g., Carpenter et al., 2016). The frictional creep relaxation ($\Delta\mu_{\text{creep}}$) differs between the two gouges showing a greater relaxation for the ANH/DOL gouge when compared to quartz gouge (Figure 5b). Details on the evolution of gouge layer thickness during the two stages of hold (Δh_{creep}) and reshear ($\Delta h_{\text{re-shear}}$) can give us important information on the micromechanical processes at the origin of frictional healing (see Figures 5c and 5d). We find that ANH/DOL has a greater compaction rate (Δh_{creep}) during the hold period when compared with quartz, resulting in a higher frictional creep relaxation (Figures 5b and 5d). Furthermore, upon reshear the ANH/DOL shows dilatant behavior that increases with the hold time and depends inversely on normal stress (i.e., at lower stress the dilation is bigger than at higher normal stress), while quartz does not show any significant dilatant behavior (Figure 5c).

Taken together, these results show that frictional healing and volumetric deformation of the fault gouges are strictly related and are different for the two gouges here investigated. The quartz behavior is almost independent on applied normal stress, and it is accompanied by small compaction during the hold stage and negligible dilation upon reshear suggesting that only a small fraction of the fault gouge is involved in deformation. The higher frictional healing rate of the ANH/DOL (Figure 3) is most likely the result of the dilational work against the normal stress, which is time-dependent and normal stress dependent.

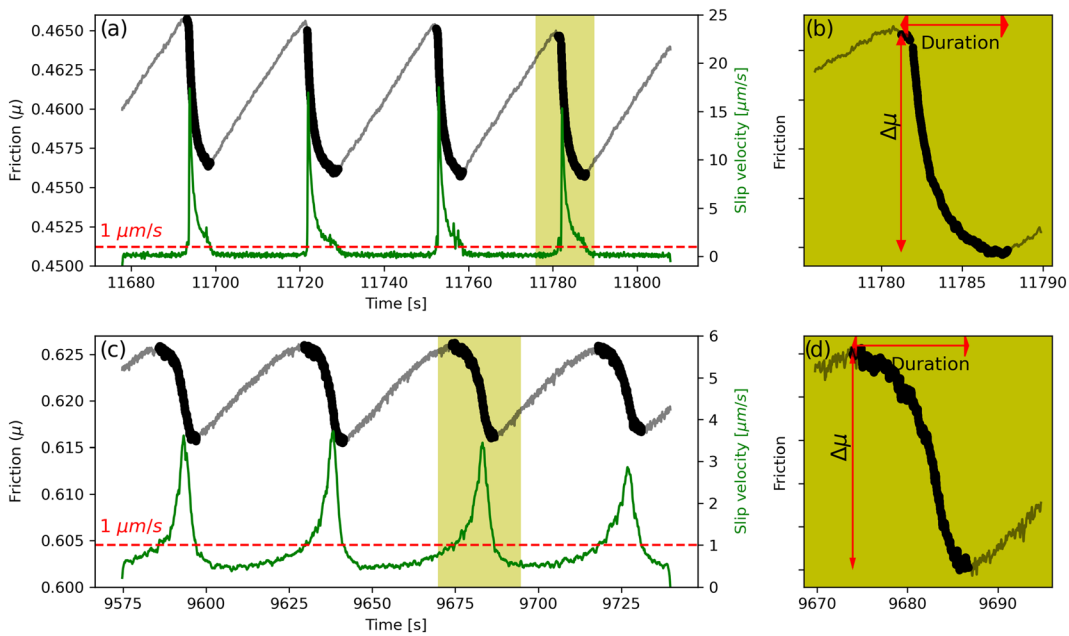

Figure 7. Time series of friction (black) and slip velocity (green) for a selected portion of the experiments. The top panels (a, b) show events for ANH/DOL, while the bottom panels (c, d) for quartz gouge. The friction drop ($\Delta\mu$, highlighted in bold) begins when the slip velocity overcomes the remotely applied loading rate (dashed red line) and terminates when the slip velocity slows down below. Panels (b) and (d) show the details of the breakdown stage for a single slow-slip event and the calculated duration and friction drop used in Figure 8.

3.3. Slow-Slip Events and Dynamic Parameters

We have reproduced slow-slip events in the laboratory by finding the appropriate boundary conditions to impose a stiffness ratio $K = k/k_c \sim 1$, following the experimental framework developed in previous studies (section 2.1) (Leeman et al., 2016; Scuderi et al., 2017). The condition $K \sim 1$, is attained, for a spring with stiffness 0.00296 [MPa/μm], for a normal stress of 15 [MPa] for the quartz gouge and 35 [MPa] for the ANH/DOL gouge. All the experiments discussed below are performed under this boundary condition of $K = k/k_c \sim 1$.

Figure 6 shows typical experimental curves highlighting the high reproducibility of the experiments. From the RSF analysis (shown in Figure 4), we found that unstable slip (i.e., velocity weakening behavior) can be obtained only at a sliding velocity of 1 μm/s for ANH/DOL gouge, while for the quartz there is a wider velocity range, so that after the initial shearing at 10 μm/s we dropped the velocity to 1 μm/s and kept it constant for the rest of the experiment (Figure 6). The quartz gouge is characterized by a steady-state coefficient of friction $\mu_{ss} = 0.64$, while the ANH/DOL shows a peak friction at $\mu = 0.7$ followed by a strain weakening stage until steady-state friction is achieved at $\mu_{ss} = 0.45$ (Figure 6). For both fault gouges, instabilities emerge spontaneously from stable sliding after the fault gouge has accumulated a typical amount of strain, 6 to 8 for ANH/DOL and 8 to 10 for quartz, indicating that a developed fault gouge microstructure is needed to host instabilities (Scuderi et al., 2017).

For each experiment, we record hundreds of unstable events and analyze them to identify the beginning and termination of each event and evaluate dynamic parameters such as friction drop, total event duration (T_d), peak slip velocity, and event slip. Figure 7 shows a portion of the experiments highlighting repetitive slow-slip events for both ANH/DOL (upper panels) and quartz (bottom panels). In general, during the interseismic phase, the fault gouge slips at velocities less than the background loading rate and friction increases linearly with time (and slip); the subsequent coseismic phase is characterized by slip acceleration and friction drop. To individuate the initiation and termination of the breakdown stage (i.e., stress drop), we determine when the slip velocity overcomes the background loading rate of 1 μm/s and when it slows down below it (Figure 7). By adopting this approach, we are able to carefully discriminate the onset and termination of each unstable event (bold curves in Figure 7). We use the information derived from this analysis to compare the dynamic parameters during unstable slip between the two fault gouges here investigated.

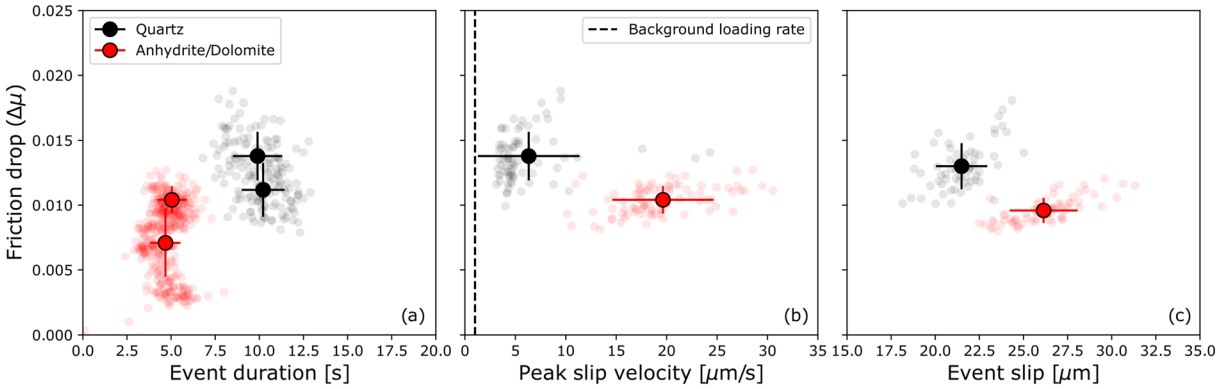

Figure 8. Summary of the results for all the experiments showing the relation between friction drop and event duration (a), peak slip velocity (b), and event slip (c). For each experiment we report the all the values for all the events analyzed (light colors) along with the mean (bold circles) and standard deviation (error bars). Only for panel (a) we reported data for two experiments for both the fault gauges.

Figure 8 shows the friction drop ($\Delta\mu$) for both ANH/DOL and quartz as a function of total event duration (T_d), peak slip velocity, and event slip. In each panel, the circle with the error bars identifies the average value and the standard deviations estimated for all the events analyzed during each experiment. The friction drop values estimated for ANH/DOL and quartz are similar and range within the interval $0.005 < \Delta\mu < 0.015$. The event durations measured for ANH/DOL are shorter (average values are around $T_d \sim 5$ s) than those for quartz (average durations of $T_d \sim 10$s). The friction drop durations are extremely longer when compared to regular stick-slip events generated in the same machine (events duration in the range of 0.003–0.004 s, Tinti et al., 2016; Scuderi et al., 2017). This is consistent with the imposed $K \sim 1$ at the transition between stable and unstable slip, characterizing laboratory slow-slip events. In agreement with this observation, the peak slip velocity for quartz (~7 μm/s) is only slightly above the imposed background loading rate (1 μm/s), and it ranges between ~10 and ~25 μm/s for ANH/DOL. This parameter also greatly differs from regular stick-slip events in which the peak slip velocities are in the order of mm/s. The slip accumulated during the coseismic event is also comparable between the two fault gouges and lies in a range between 20 and 30 μm. These experiments corroborate the evidence that slow-slip frictional sliding can occur in different geomaterials by imposing a stiffness ratio of $K \sim 1$ within the conditionally stable regime.

4. Microstructures

In order to obtain insights into the deformation processes occurring during the slow-slip events described above, we have performed a microstructural analysis at SEM of the resulting fault zone after the experiments. The quartz fault gouge is characterized by grain size reduction in the bulk volume of the fault zone (Figure 9a). Shear localization is observed along boundary shear zones (B-planes), with a thickness of ~100 μm, that contain subparallel principal slip surfaces, Y-shears, with a thickness of 3–4 μm, where the grain size reduces to ≤1 μm (Figures 9a and 9b, Scuderi et al., 2017). The Y-shear planes are continuous within the B-planes and have an almost planar geometry. Moving away from the Y-planes, we observe a gradual increase in grain size testifying that while most of the energy for slip is spent along these principal slip surface, some energy is also consumed away of Y-planes resulting in a gradual reduction in the grain size (Figures 9c and 9d).

The ANH/DOL is characterized by a heterogeneous structure due to the contrast in mineral strength, where the anhydrite represents a weak phase when compared to the stronger dolomite (Figure 10). The microstructure consists of well-developed boundary shear zones (~200 μm thick), characterized by grain size reduction with grains of dolomite, usually with a subrounded shape, that ranges in size from a few tens of microns to submicron and dismembered grains of anhydrite of much smaller size. In some places, the boundary shear planes merge into a P-foliation that develops across the bulk volume of the gouge (Figure 10a). The P-foliation is mainly characterized by fine grained, dismembered anhydrite grains that in some cases

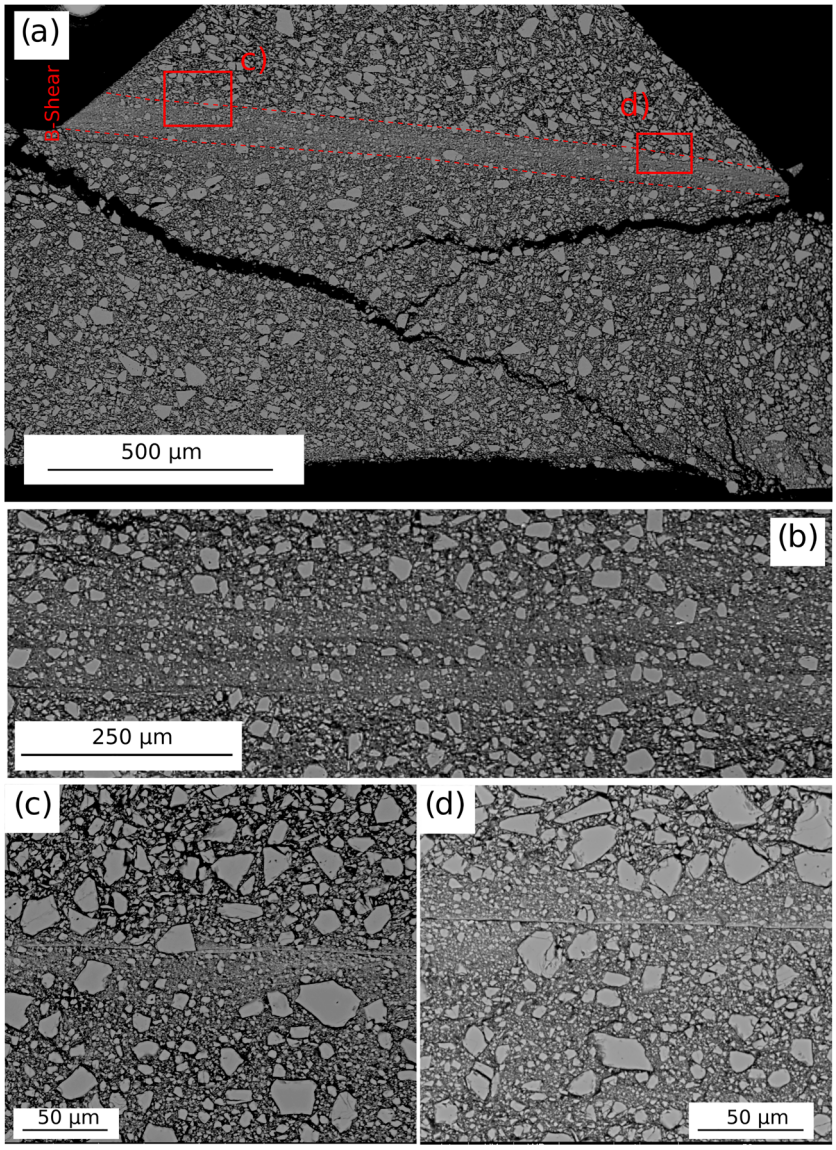

Figure 9. Resulting fault gouge microstructures for the quartz gouge. (a) Deformation is mainly localized with boundary shear planes (B-shear) characterized by intense grain size reduction when compared to the bulk volume of the gouge. (b) Details of the B-shear where multiple *Y* planes are subparallel and continuous. (c, d) Details of shear localization along Y-shear planes observed within the B-shear plane.

surround bigger clasts of dolomite that have angular shape and, in most cases, present fractures (Figures 10a and 10b). In some places, fractures within anhydrite allow for a sort of boudinage along the P direction; close to the termination of the shear zone, the anhydrite-rich P planes present drag folds consistent with the sense of shear (Figures 10b and 10d). Within the B-planes, we observe shear localization along discontinuous surfaces mainly characterized by very fine dolomite grains (Figure 10c). It is evident that the two mineralogical phases tend to separate as a result of shear deformation due their different strength, testifying that shear strain is heterogeneously partitioned.

The comparison of the two experimental faults indicates that while in quartz the deformation is localized along a limited fault volume represented by 3–4 µm thick Y-shear planes, in ANH/DOL the deformation is mainly distributed through the entire fault volume.

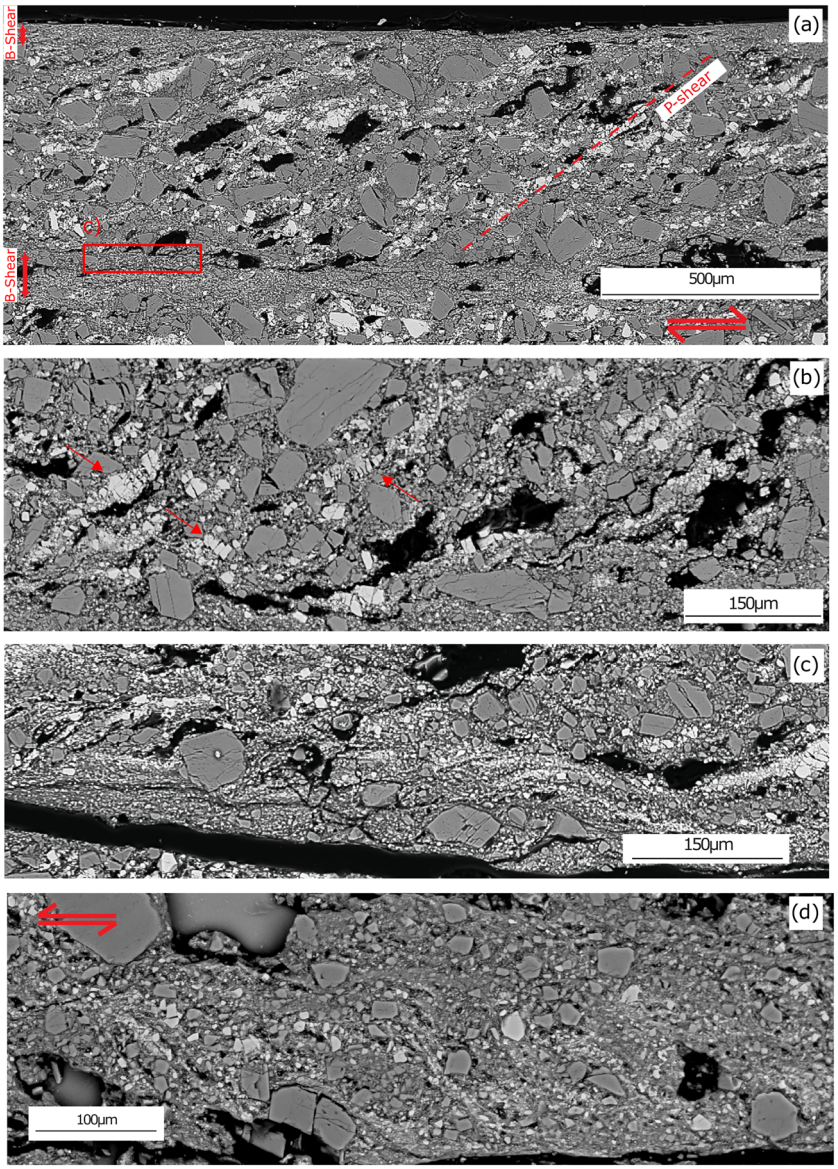

Figure 10. Resulting fault gouge microstructure for the ANH/DOL gouge (anhydrite is in light color, while dolomite is darker). (a) Deformation is localized along thick boundary shear planes (B-shear) where grain size reduction is observed. The boundary shears are connected by a P-shear foliation. Panel (b) shows details of P-shear foliation (red arrows show the details of anhydrite deformation). Panels (c) and (d) show details of shear accommodation within the boundary shear planes. (c) Anhydrite grains are dismembered and for an anastomosed fabric. (d) S-C type foliation is commonly observed within the boundary shears.

5. Discussion

Our results indicate that there is an intimate relationship between the dynamical attributes of laboratory slow-slip events, such as the evolution of friction and slip velocity and the fault zone structure. For both the fault gouges used in this study, a finite amount of strain is required before the spontaneous onset of frictional instabilities (Figure 6). This observation suggests that strain localization is a requirement to create the mechanical conditions to host frictional instabilities.

5.1. The Anatomy of Laboratory Slow-Slip Events

In this section, we analyze the relation between friction, slip velocity, and layer thickness (i.e., volumetric deformation) to unravel the details of fault gouge deformation during slow-slip frictional sliding. Figure 7

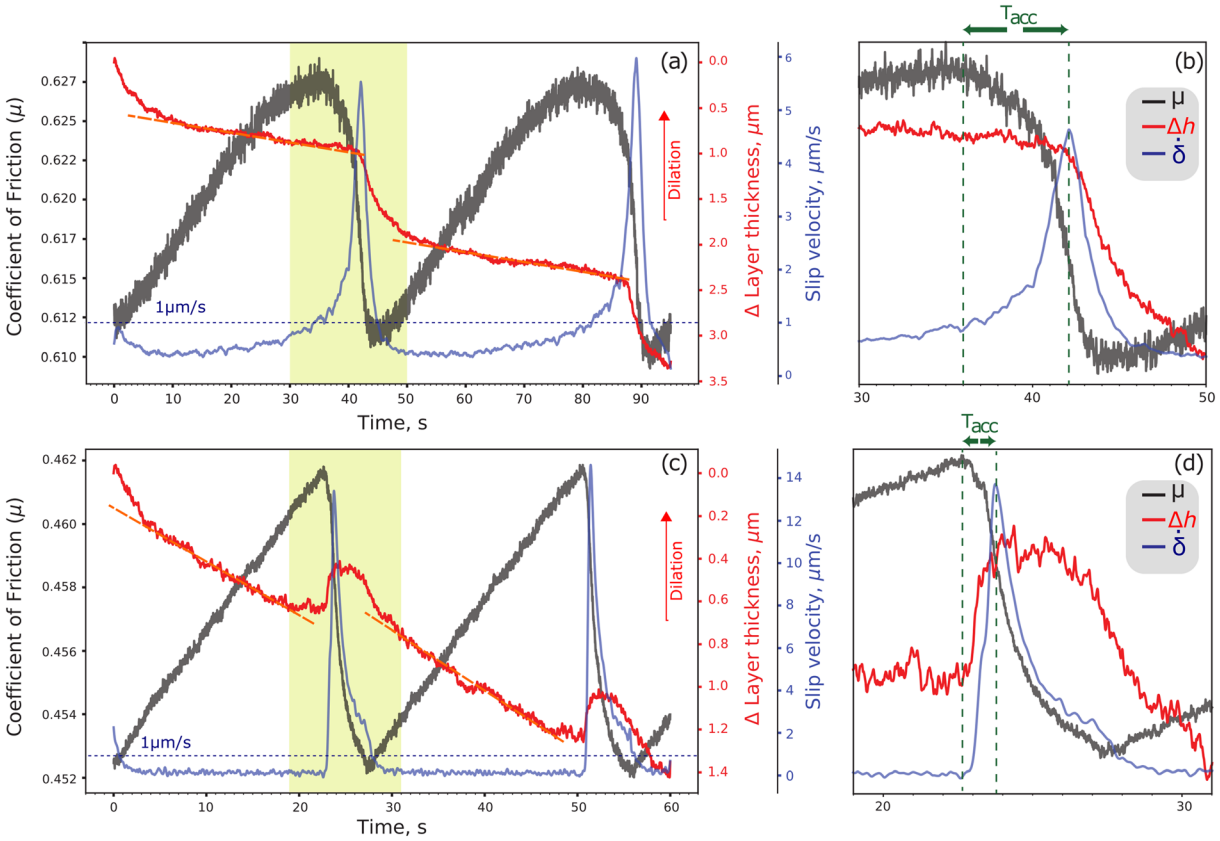

Figure 11. Details of slow-slip events for quartz (top row) and ANH/DOL (bottom row). Panels (a) and (c) show the time series of friction (black) slip velocity (blue) and layer thickness (red, compaction negative) for two representative events. The blue dashed lines represent the background loading rate of 1 μm/s, and the orange dashed lines represent the best fit of the linear evolution in layer thickness. Panels (b) and (d) show the expansion of the signals within the yellow boxes in panels (a) and (c).

shows the repeated sequence of frictional instabilities for quartz (bottom panels) and ANH/DOL (upper panels) fault gouges. A first visual analysis of these time series indicates that the evolution of friction and slip velocity is quite different for the two fault gouges. Slip acceleration to peak slip velocity and the onset of the friction drop for the ANH/DOL gouge take place in a relatively short duration (usually ≈1.5 s), and it is followed by a longer stage during which the slip velocity slows down to the background loading rate at the end of the friction drop. The resulting evolution of friction drop (i.e., breakdown stage) is characterized by a concave decay with time followed by a sudden restrengthening (i.e., friction increase) causing the termination of slip. The relation between friction drop and slip acceleration for the quartz gouge is more complex. The slip velocity begins to evolve gradually around the yield stress (i.e., preseismic creep) until the peak slip velocity is attained toward the end of the breakdown stage. The resulting friction drop displays a convex shape for most of the duration of the breakdown stage characterizing the instability.

In order to shed light on the mechanical processes that can be at the origin of the frictional instabilities during laboratory slow-slip events, we show in Figure 11 the temporal evolution of friction, slip velocity, and the correspondent volumetric deformation for two typical slow-slip events generated in both fault gouges. The slip cycle during each slow-slip event is characterized by a linear stress increase (here represented by friction evolution) with time (interseismic stage), during which the fault is under quasi-stationary contact and the slip velocity is slower than the background loading rate (i.e., <1 μm/s) (Figures 7 and 11). During this stage, the fault gouge compacts allowing for contact healing and restrengthening. This is common to both fault gouges. However, while during the interseismic stage the slip velocity for ANH/DOL is basically zero and the fault is locked until the onset of the instability, the quartz gouge shows a nearly continuous slip evolution with a clear preseismic creep preceding the main slip acceleration associated with the frictional instability (Figures 11a and 11b, Scuderi et al., 2016).

The peak in fault friction marks the onset of the frictional instability (coseismic stage) corresponding with the onset of slip acceleration. During this stage, the two fault gouges show a markedly different behavior (Figure 11). On the one hand, the friction drop for quartz starts gradually with a gentle rollover followed by a more pronounced drop (Figure 11b). The corresponding evolution of the slip velocity shows an exponential evolution, resembling tertiary creep, corresponding to the convexity of the friction curve and followed by a faster acceleration yielding peak slip velocity. It results that slip acceleration is long, T_{acc} ~ 6 s, representing more than half-duration of the whole breakdown process. During this stage, the fault gouge compacts at the same volumetric rate as during the preseismic stage (Figure 11a). The peak slip velocity is reached when the breakdown stage is nearly concluded with friction close to its minimum before restrengthening and slip termination (Figure 11b). At the onset of slip deceleration, the fault shows an abrupt increase in compaction rate that persists until the beginning of the next cycle allowing fault deceleration and contact healing. The change in volumetric deformation is indicative of a change in the micromechanical processes that accommodate shear deformation within the fault gouge that is clearly captured in the source time function that resembles a Gaussian slip velocity function. On the other hand, the ANH/DOL fault gouge shows a faster decrease in friction at the onset of unstable slip, associated with a sharp slip acceleration followed by a gradual slip deceleration (Figures 11c and 11d). The slip velocity is characterized by an acceleration phase with a duration T_{acc} ~ 1.5 s. In this case, the slip velocity function resembles a Yoffe function which is commonly used in kinematic modeling of recorded ground motions to simulate the rupture propagation during earthquakes (e.g., Tinti et al., 2005). The corresponding volumetric deformation shows that at the onset of the instability, when slip accelerates, the fault dilates reaching the maximum value in the vicinity of the peak slip velocity (lasting T_{acc}). After the peak in slip velocity, the gouge layer deforms at a nearly constant layer thickness and then starts to compact again at a greater rate (until the end of the coseismic phase) when compared to the compaction during the interseismic stage (Figure 11c). These observations suggest that fault gouge composition and the resulting fault structure play an important role in controlling the mechanisms of strain energy release during the coseismic stage via different micromechanical processes that are captured in the slip velocity function during slow-slip events. From these results emerge that the slip velocity evolution during frictional instabilities contains key information about the dynamics of slow-slip events.

Our observations during SHS tests, used to mimic the seismic cycle, agree with the fault slip behavior observed during slow-slip events. In fact, the high frictional healing rate observed for ANH/DOL (Figure 5a) would favor fault restrengthening by locking the fault during the interseismic stage, with the entire volume of the gouge involved in compaction and internal deformation (Figure 5d). During reshear in SHS test, we report a time-dependent dilatant behavior that is also observed during the coseismic stage of slow-slip events, suggesting that for this fault gouge dilation is an efficient mechanism to dissipate energy during unstable slip. Dilation is also favored by the larger grain size of the ANH/DOL mixtures in comparison to quartz, for example, Figure 9 versus Figure 10. On the contrary, the low healing rate and the absence of dilation during reshear in quartz SHS experiments are well coupled with the creep-slip behavior that we observe during slow-slip events accompanied by a persistent compaction (Figures 3 and 5).

5.2. Dynamics of Slow Frictional Sliding

Figure 12 shows the slip weakening curves (friction versus coseismic slip) and the evolution of the layer thickness with slip for a set of representative slow-slip events (panels a and c) together with the associated phase diagrams (panel b and d). For the sake of simplicity and to facilitate the comparison, we offset to zero the value of slip at the beginning of each cycle of frictional instability. Blue circle highlights the occurrence of the peak slip velocity for each event and green circle the deviation from linear loading.

The quartz gouge shows a linear friction increase over a cumulated slip of ~10 μm followed by nonlinear increase up to the peak friction for a total cumulated slip of ~20 μm during the interseismic phase. This is followed by a friction drop (Figure 12a) characterizing the breakdown stage. As anticipated above, the peak slip velocity for quartz gouge is reached more than halfway in the breakdown stage. This feature is clearly shown by the phase diagram in Figure 12b. Worthy of note, the sudden increase in compaction rate starts at the peak slip velocity and corresponds to the coseismic deceleration (Figures 12a and 12b), suggesting that there is an evolution in the micromechanical processes accommodating deformation during the breakdown stress drop. By coupling these mechanical information (Figures 11 and 12) with the resulting fault zone structure (Figure 9), we can infer the dynamics of frictional sliding during slow-slip events. The deviation

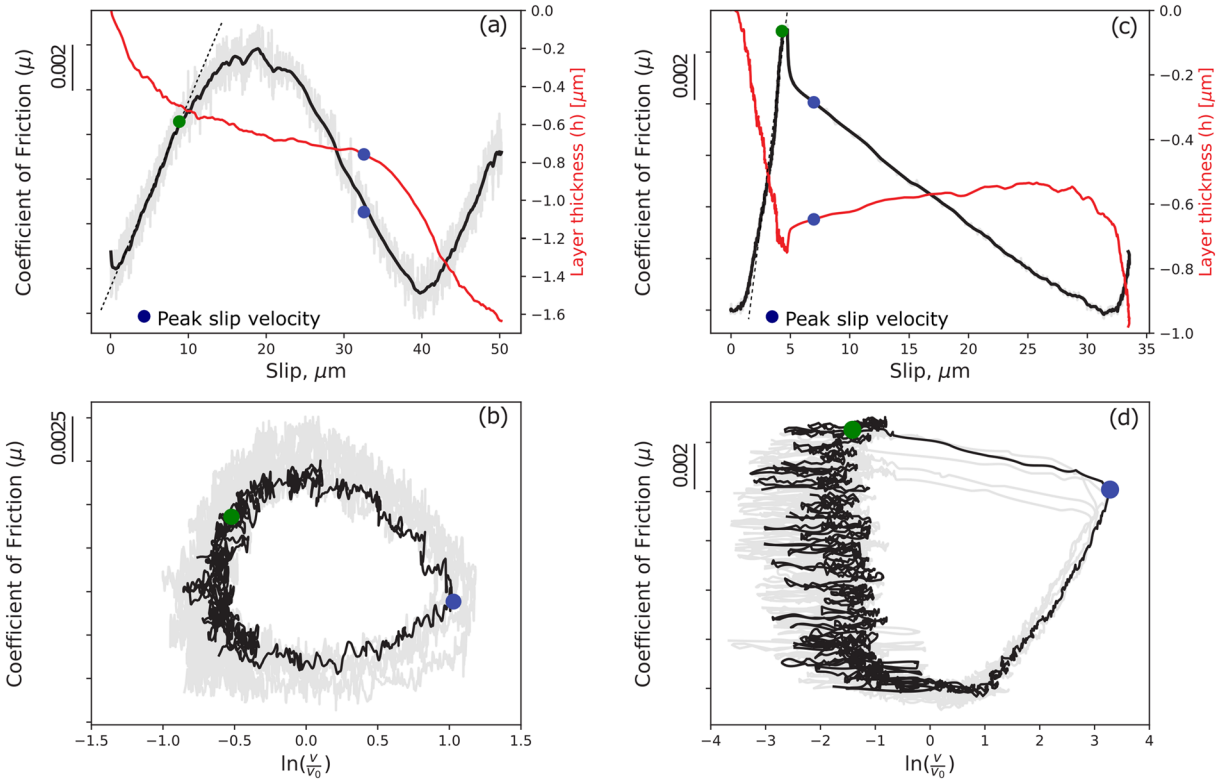

Figure 12. Top panels (a, c) shows slip weakening curves (i.e., friction vs. slip) for quartz (panel a) and ANH/DOL (panel c) along with the evolution of the gouge layer thickness (red curves). The dashed lines represent linear loading, and the green circle marks the departure from it. The blue circle represents the occurrence of the peak in slip velocity. Bottom panels (b, d) show the associated phase plane diagram for quartz (panel b) and ANH/DOL (panel d).

from the linear loading (green circle in Figures 12a and 12b) marks the onset of preseismic creep and an evolution in the compaction rate from a nonlinear high rate to a lower rate almost linear. The compaction rate remains constant throughout the first portion of the breakdown stage, up to the peak in slip velocity. We posit that while the compaction rate is constant (i.e., from the green to blue circle) sliding is likely accommodated along the Y-shear planes contained within the B-shear zones of the fault gouge (Figure 9b). The Y-shear planes represent continuous and very thin planes of weakness where slip is energetically favored resulting in a shear deformation at almost constant layer thickness given that the fault is accelerating and frictional strength is decreasing (i.e., velocity weakening) (e.g., Beeler et al., 1996; Marone et al., 1990). Then, as the fault decelerates, and the shear strength is almost at its minimum, deformation tends to be more distributed across the gouge causing shear delocalization and cataclastic processes in the vicinity of the slipping zone, manifested in a higher compaction rate. The microstructure also shows a gradual increase in grain size above and below the Y-shear planes (Figures 9b and 9c). The phase diagram for quartz gouge shows subrounded (or egg shaped) trajectories similar to those reported by Leeman et al. (2018) for both experimental data and 1-D spring-slider model. The preseismic phase is characterized by a smooth slip acceleration associated with the friction hardening phase (creep-slip event) followed by a coseismic acceleration associated with friction drop. Such type of trajectory implies that the "state variable" (θ) is unsteadily evolving in a thin volume surrounding the principal slipping planes where strain is localized resulting in a never truly locked fault, describing a creep-slip type of frictional sliding. This interpretation is also supported by the observation that the quartz gouge always shows a velocity weakening behavior (Figures 4a and 4b) that would imply shear along localized slip planes (e.g., Beeler et al., 1996; Marone, 1998; Scuderi et al., 2017), low healing rate, and no dilatant behavior upon reshear during SHS test (Figures 3 and 4c).

The ANH/DOL also shows an evident slip weakening behavior characterized by a linear increase of friction over a smaller amount of slip (~5 μm) when compared to quartz during the interseismic phase, which is

followed by a two stages friction drop (Figure 12c), the first one from the peak friction to the friction value associated with peak slip velocity and the subsequent one from that friction value up to the minimum friction. Most of the slip during the breakdown stage occurs during the slip deceleration from peak slip velocity associated with the largest friction drop. The phase diagram (Figure 12d) clearly shows that peak slip velocity is reached over a relatively small amount of slip with a modest friction drop. We note that this behavior is not predicted by theoretical dynamic simulations based either on slip weakening law or RSF (e.g., Bizzarri et al., 2001; Fang et al., 2010; Tinti et al., 2005). The coupling of the volumetric deformation with the microstructural observations can shed light on the dynamics of these slow-slip events. During the interseismic stage, the fault compacts and accumulates elastic strain energy (Figure 12c). The peak in friction marks the onset of the coseismic stage that begins with a marked increase in slip velocity due to the accumulated elastic energy. Simultaneously, with slip acceleration the fault begins to dilate. Dilation is a common mechanism observed in fault gouge that dissipates strain energy and tends to stabilize slip (e.g., Beeler et al., 1996; Mandl et al., 1977; Marone et al., 1990). Dilation in the ANH/DOL is favored by a heterogenous fault zone structure lacking a pervasive zone of shear localization suggesting that during the breakdown phase slip is more distributed and possibly also accommodated along the S-C foliation producing dilational work against the normal stress. We also observe pervasive fracturing, that is an important dilatant mechanism consuming energy, within the anhydrite grains, that appears as dismembered, and some fractures within the dolomite grains. In addition, the larger grain size of the ANH/DOL in comparison to quartz contributes in facilitating dilation. Dilation is associated with a modest amount of slip, and most of the mechanical work is absorbed during the deceleration phase. This behavior is consistent with the SHS data (Figure 5) showing a significant frictional healing for ANH/DOL and, upon reshear, a marked dilation. Also, the evolution of the stability parameter (a-b) from velocity weakening at slow-slip rate to velocity strengthening at higher slip rates suggests that pervasive fault deformation would favor the stabilization of slip (Figure 4c) (e.g., Beeler et al., 1996; Fagereng et al., 2014). This mechanism is appealing since dilation could act in concert with variation in porosity and perhaps pore pressure to further quench the instability, as it has been proposed by theoretical model (e.g., Liu, 2013; Segall et al., 2010) and inferred from outcrop observations (e.g., Fagereng et al., 2014).

The trajectories of phase diagram (highly reproducible across experiments under the same boundary conditions) show points of consensus and some discrepancies when compared to theoretical models of earthquake rupture based on RSF or slip weakening laws. For quartz gouges the occurrence of the peak slip velocity approximately at the end of the breakdown stage (Figure 12) is consistent with theoretical models of earthquakes and stick-slip events observed on planar surfaces (e.g., Fang et al., 2010; McLaskey, 2019; Mclaskey & Yamashita, 2017). Similarly, the assumption in these theoretical models of a medium that is perfectly elastic with an infinitesimal surface of discontinuity is quite similar with the sharp zone of localization observed in quartz gouges and our interpretation that the coseismic acceleration takes place along these planes (Figure 9). For ANH/DOL the achievement of the peak slip velocity after a very small drop in friction is not predicted by theoretical models as well as the long deceleration stage, emphasizing the importance of shear strain partitioning in a heterogenous fault gouge associated with fault dilation.

5.3. Coseismic Phase and Breakdown Work

The results discussed above indicate that the mechanical response of the two fault gouges during the breakdown stage might be associated to different micromechanical processes that dissipate the accumulated strain energy within the volume subjected to shearing and containing the slipping zones. In terms of dynamic parameters our results, shape of the friction drop and slip velocity time histories corroborate the different response of the fault gouge and highlight the role of fault fabric during slow-slip instabilities.

In order to further understand the different response and the dynamic processes occurring during the coseismic breakdown stage, we have computed the mechanical work absorbed during frictional instabilities associated with slow-slip events. The two top panels in Figure 13 show the traction evolution (black curves) and the slip velocity evolution (red curves) as a function of slip. For sake of simplicity we assume zero slip at the beginning of each coseismic phase. The shaded area below each slip weakening curve (from the beginning of the coseismic phase) represents the breakdown work, interpreted as an estimate of the mechanical work absorbed on a virtual mathematical plane of zero thickness, describing the fault zone during the coseismic rupture (e.g., Cocco & Tinti, 2008; Tinti et al., 2005). The breakdown work is defined as the excess of work

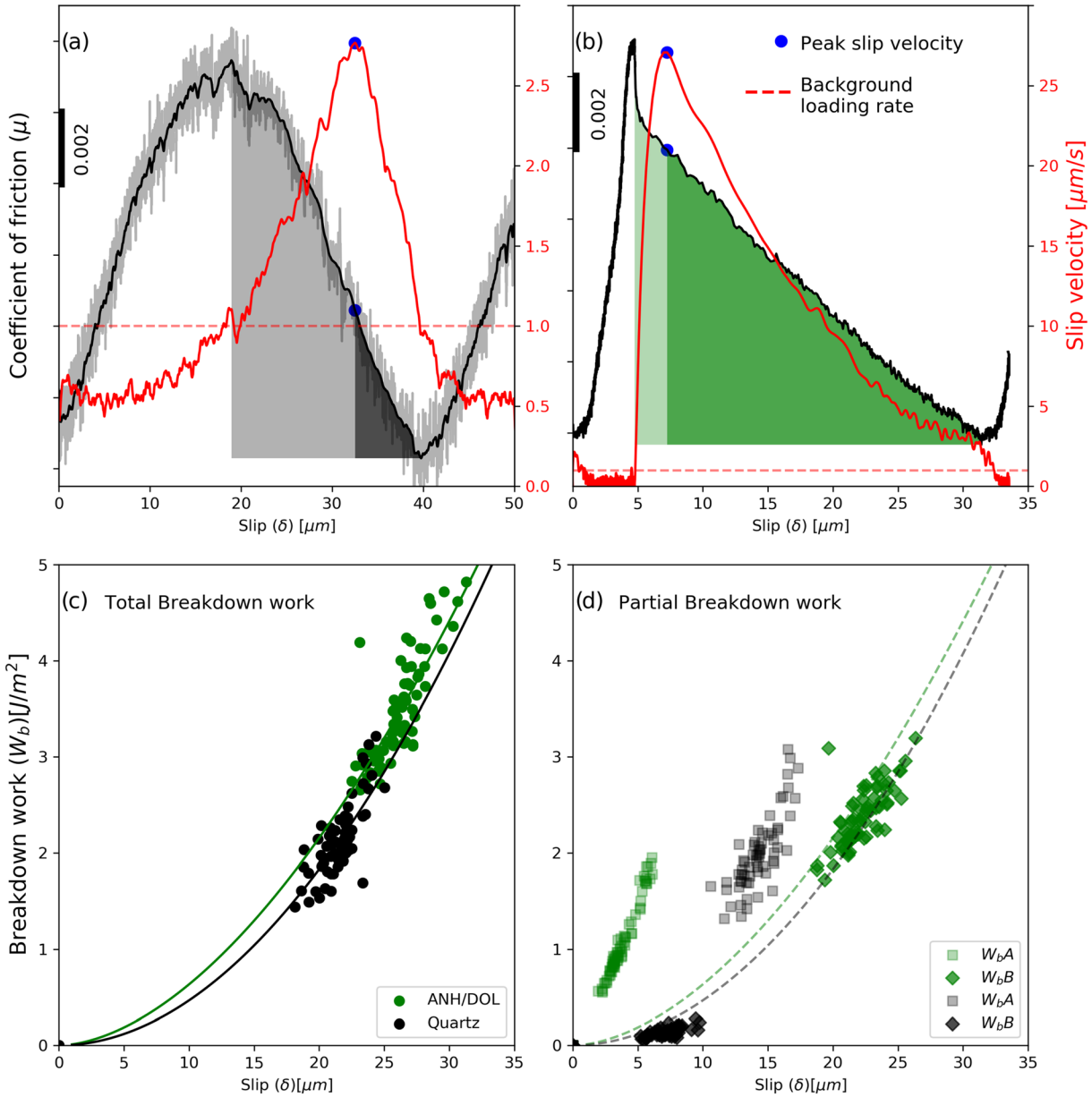

Figure 13. Top panels show the slip weakening curves (black) and slip velocity (red) for quartz (a) and ANH/DOL (b). The shaded areas below the friction curves represent the breakdown work calculated before the peak slip velocity (light shaded) and after (dark shaded). The bottom panels show the scaling of total breakdown work as a function of event slip for all the slow-slip events investigated (c) and the values of the partial breakdown work calculated before the peak slip velocity (squared) and after (diamonds) (d). The lines in panels (c) and (d) represent the best fit performed with a power law: The retrieved exponents agree with previous literature (Viesca & Garagash, 2015) being 1.97 for quartz and 1.76 for ANH/DO.

over the traction level having minimum magnitude ($\mu_{\min}$) achieved during slip. Breakdown work is an energy density (J/m^2). The total breakdown work in each panel is split into two portions (identified by different colors): the breakdown work absorbed before (W_{bA}) and after (W_{bB}) the occurrence of peak slip velocity (shown in Figures 13a and 13b by the blue dots). In this analysis we neglect the contribution of the preseismic slip observed in quartz for simplicity, but we posit that it might have a role in the energy budget for that fault gouge. The time and slip necessary to reach peak slip velocity are different in the two materials (see Figure 11), showing a different duration of the acceleration time T_{acc} and a different ratio T_{acc}/duration (this ratio for quartz is 2–3 times greater than for ANH/DOL). The two bottom panels show the scaling of the estimated breakdown work values (total W_b and partial W_{bA} and W_{bB}, respectively) as a function of accumulated slip.

For the quartz a relevant portion of the mechanical work is absorbed before that slip velocity reaches its peak and before the high compaction phase (see Figure 11). Indeed, the high rate of compaction for quartz coincides with the deceleration phase of slip velocity. Differently, for the ANH/DOL, the larger portion of the mechanical work is absorbed after the slip velocity reaches its peak (during the slip deceleration and healing of slip), while the high dilation rate is observed before the occurrence of peak slip velocity (see Figures 11 and 12). For quartz the temporal evolution of the quantities shown in Figure 11 (friction, slip velocity, layer thickness) suggests that the energy is mainly absorbed during the propagation along the well-localized plane of rupture, and at the end of the coseismic phase, a limited amount of work is absorbed "off-fault" during the significant compaction phase (as inferred by the distribution of grain size reduction in microstructural analysis shown in Figure 9). The mechanical work during this latter phase is negligible as well as the corresponding slip suggesting that the fault starts to heal (Figure 13). Differently, for the ANH/DOL, the dilation processes associated with slip acceleration require a relatively modest portion of the breakdown work, likely absorbed in a 200 μm thick shear zone (e.g., Figure 10c), while most of the breakdown work is absorbed during the deceleration stage. This might also suggest the existence of competitive processes occurring in a larger volume surrounding the slipping zones, that is, slip along the shear zone versus shearing along the foliation with the breaking of anhydrite grains and granular flow (causing local dilation).

The scaling of total breakdown work with slip (Figure 13c) follows the same scaling inferred for the seismological fracture energy G′ computed for point sources (see the curves in Figure 13c) (Abercrombie & Rice, 2005) and for the breakdown work for extended sources (Cocco et al., 2016; Tinti et al., 2005, and references therein). The values of the total breakdown work inferred in this study for slow-slip events match the scaling retrieved for earthquakes independently of the modeling assumptions to estimate and interpret the measures. This implies that, from an energy point of view, the involved physical processes require a similar mechanical work for slow-slip events and regular earthquakes. The scaling of the partial breakdown work estimates calculated before (square) and after (diamond) the peak slip velocity is shown in Figure 13d. This figure shows that for ANH/DOL the breakdown work before peak slip velocity is associated with very small values of slip, while for quartz the slip is larger but the stress drop associated with the breakdown work after peak slip velocity is extremely small compared with those inferred for the slip acceleration stage.

6. Conclusions

We have performed experiments in a double-direct biaxial shear apparatus and used two different fault gouges, quartz powders, and a mixture of anhydrite and dolomite 50–50 wt% (ANH/DOL) to test the role of fault heterogeneity in the breakdown processes of slow-slip events. Slow-slip events arise spontaneously from stable sliding under the specific boundary condition of a stiffness ratio $K = k/k_c \sim 1$, as described in previous works (e.g., Leeman et al., 2016, 2018; Scuderi et al., 2016; Tinti et al., 2016). The slow-slip events show comparable absolute values of total friction drop, duration, peak slip velocity, and cumulated slip testifying that the RSF constitutive framework can be used to describe slow-slip events in different geomaterials. The result is that laboratory slow-slip events represent frictional instabilities and obey the same constitutive laws as regular earthquakes, suggesting that they may be governed by similar physical mechanisms, contributing to the continuum fault slip behavior. This observation agrees with the wide range of tectonic environments where slow slip is observed (e.g., Peng & Gomberg, 2010) providing a general frictional framework, determined by the variation of k and k_c depending on the local boundary conditions (e.g., Brantut et al., 2011).

We have documented that heterogeneities in fault mineralogical composition and the resulting fault zone structure have a strong control on the coseismic breakdown processes. We find an intimate relationship between the slip velocity function and the volumetric fault deformation that is controlled by shear localization and strain partitioning within the fault gouge. Slip velocity time histories inferred for quartz are characterized by creeping and a progressive acceleration to peak slip velocity ($T_{acc} \sim 6$ s) followed by deceleration toward the background sliding velocity having a shorter duration than the slip acceleration stage. Differently, the slip velocity time histories inferred for ANH/DOL show a relatively short acceleration to peak slip velocity ($T_{acc} \sim 1.5$ s) followed by a progressive deceleration to the background sliding velocity. As a result, the total slip duration (T_d) documented for quartz ($T_d \sim 10$ s) is longer than the one obtained for ANH/DOL (~5 s); this is mainly due to the presence of creeping before the slip acceleration to peak slip velocity. The ratio between the acceleration time (T_{acc}) and the total slip duration (T_d) for quartz is 2–3 times

greater than for ANH/DOL. The evolution of volumetric deformation observed during the laboratory experiments also shows remarkable differences for the two fault gouges, which we interpreted in the light of the microstructural analyses. In detail, the creep-slip behavior associated with the persistent compaction that we observe for quartz suggests that strain energy is absorbed to allow slip along highly localized planes until the peak slip velocity. The increase in compaction rate during deceleration can result from cataclastic processes and grain size reduction away from the localized slipping plane. Differently, the coseismic fault dilation observed for the ANH/DOL gouge that occurs simultaneously with slip acceleration and is likely due to slip partitioning and local normal stress changes within the entire experimental fault during the coseismic phase. Noteworthy, the compacting behavior observed during the interseismic phase for ANH/DOL corresponds to a small amount of slip (i.e., the fault is locked) and has larger absolute values than the dilatant behavior recorded during the coseismic phase. It is significant that the micromechanical processes are strongly coupled with slip velocity evolution showing an evident relationship during the coseismic breakdown stage. Our results suggest that multiple processes, which may act in concert and depend on the internal structure of the fault, can explain the occurrence of slow-slip events. On the one hand, the observations of volumetric dilation during the breakdown stage (friction drop) reported for ANH/DOL are consistent with the dilation-strengthening mechanism (Segall et al., 2010). On the other hand, when shear is highly localized as in quartz gouge, the friction drop is accompanied by compaction that is in contrast with the dilation-strengthening mechanism but may still agree with a designer friction law where the RSF constitutive parameters change as a function of slip rate (e.g., Leeman et al., 2018; Rubin, 2011).

The results presented in this study indicate that under similar loading conditions (i.e., $K \sim 1$) the two fault gouges dissipate the accumulated strain energy during coseismic slip by different mechanical processes within the volume undergoing shearing that contains the slipping zones. For quartz, most of the mechanical work is absorbed during the acceleration to peak slip velocity, requiring ~68% of the total slip due to accelerated creep along well-defined slip planes governing the friction evolution around the yield stress level (i.e., peak friction) and during most of the subsequent breakdown stage. In this stage, the rock sample is compacting at constant rate, suggesting that slip is highly localized. Slip deceleration to the background loading rate is associated with a marked increase in compaction rate, luckily associated with micromechanical processes of shear delocalization such as grain size reduction outside the zone of localized slip that require a small amount of mechanical work. For ANH/DOL slip acceleration to peak slip velocity requires a modest amount of breakdown work since slip is limited to ~10% of the total slip and it is synchronous to fault dilation. The majority of the breakdown work is absorbed during the slip deceleration stage associated with most of the coseismic slip and nearly no compaction. When slip returns to the background sliding velocity, the whole bulk volume starts to compact again. These observations suggest that mechanical work is absorbed in the two fault gouges in different ways and likely by different mechanical processes within the fault core. Once the fault has developed a shear fabric capable of hosting instabilities, during the initial stages of the experiment, mechanical work is absorbed by strain rate partitioning within the structural elements during each slow-slip event. For ANH/DOL, during the breakdown stage, slip is distributed in a thick fault core, where shearing also along S-C foliation and grain fracturing can produce dilation work against the normal stress. The larger grain size of the ANH/DOL in comparison to quartz and more importantly the rheological contrast between anhydrite and dolomite contributes in creating a heterogenous fault fabric that facilitates dilation. It is impossible to determine if dilation is triggering coseismic slip or, on the contrary, if local normal stress changes causing fault instability and slip are producing dilation in the fault core. Notwithstanding, the important result is that, for ANH/DOL, we observe coseismic dilation during a slip weakening response of the fault gouge (Figure 13b).

The results in terms of slip velocity time histories corroborate the different response of the fault gouge and the role of fault fabric in contributing to the heterogeneities of fault slip behaviors. The inferred values of breakdown work W_b scale with slip following the same power law retrieved in the literature for "regular" earthquakes. This implies that the involved distinct mechanical processes require a similar mechanical work for slow-slip events and "regular" earthquakes.

Conflict of Interest

The authors declare no competing financial interests.

Data Availability Statement

Correspondence and request for additional material should be addressed to Marco M. Scuderi (marco.scuderi@uniroma1.it). The experimental time series, both raw data and analyzed, as well as the codes that have generated the figures are available at https://doi.org/10.5281/zenodo.3898725 under the open access creative commons attribution 4.0 international license.

Acknowledgments

We thank C. Marone for discussion regarding this work. D. Mannetta (La Sapienza university of Rome) and M. Albano (CNR) are thanked for help with thin section and technical assistance at the SEM, respectively. This research was supported by Sapienza Grant Ateneo 2018 to C. C. and Horizon 2020 innovation program under the Marie Sklodowska-Curie 656676 FEAT to M. M. S.

References

Abercrombie, R. E., & Rice, J. R. (2005). Can observations of earthquake scaling constrain slip weakening? *Geophysical Journal International*, *162*(2), 406–424. https://doi.org/10.1111/j.1365-246X.2005.02579.x

Ando, R., Nakata, R., & Hori, T. (2010). A slip pulse model with fault heterogeneity for low-frequency earthquakes and tremor along plate interfaces. *Geophysical Research Letters*, *37*, L10310. https://doi.org/10.1029/2010GL043056

Barnes, P. M., Wallace, L. M., Saffer, D. M., Bell, R. E., Underwood, M. B., Fagereng, A., et al. (2020). Slow slip source characterized by lithological and geometric heterogeneity. *Science Advances*, *6*(13), 1–11.

Beeler, N. M., Tullis, T. E., Blanpied, M. L., & Weeks, J. D. (1996). Frictional behavior of large displacement experimental faults. *Journal of Geophysical Research*, *101*(B4), 8697–8715. https://doi.org/10.1029/96JB00411

Behr, W. M., Kotowski, A. J., & Ashley, K. T. (2018). Dehydration-induced rheological heterogeneity and the deep tremor source in warm subduction zones. *Geology*, *46*(5), 475–478. https://doi.org/10.1130/G40105.1

Bizzarri, A., Cocco, M., Andrews, D. J., & Boschi, E. (2001). Solving the dynamic rupture problem with different numerical approaches and constitutive laws. *Geophysical Journal International*, *144*(3), 656–678. https://doi.org/10.1046/j.1365-246X.2001.01363.x

Blanpied, M. L., Marone, C., Lockner, D. A., Byerlee, J. D., & King, D. P. (1998). Quantitative measure of the variation in fault rheology due to fluid–rock interaction. *Journal of Geophysical Research*, *103*(B5), 9691–9712. https://doi.org/10.1029/98JB00162

Boatwright, J., & Cocco, M. (1996). Frictional constraints on crustal faulting. *Journal of Geophysical Research*, *101*(B6), 13,895–13,909. https://doi.org/10.1029/96JB00405

Brantut, N., Sulem, J., & Schubnel, A. (2011). Effect of dehydration reactions on earthquake nucleation: Stable sliding, slow transients, and unstable slip. *Journal of Geophysical Research*, *116*, B05304. https://doi.org/10.1029/2010JB007876

Bürgmann, R. (2018). The geophysics, geology and mechanics of slow fault slip. *Earth and Planetary Science Letters*, *495*, 112–134. https://doi.org/10.1016/j.epsl.2018.04.062

Carpenter, B. M., Ikari, M. J., & Marone, C. (2016). Laboratory observations of time-dependent frictional strengthening and stress relaxation in natural and synthetic fault gouges. *Journal of Geophysical Research: Solid Earth*, *121*, 1183–1201. https://doi.org/10.1002/2015JB012136.Received

Cocco, M., Tinti, E., & Cirella, A. (2016). On the scale dependence of earthquake stress drop. *Journal of Seismology*, *20*(4), 1151–1170. https://doi.org/10.1007/s10950-016-9594-4

Cocco, M., & Tinti, E. (2008). Scale dependence in the dynamics of earthquake propagation: Evidence from seismological and geological observations. *Earth and Planetary Science Letters*, *273*(1–2), 123–131. https://doi.org/10.1016/j.epsl.2008.06.025

Collettini, C., di Stefano, G., Carpenter, B., Scarlato, P., Tesei, T., Mollo, S., et al. (2014). A novel and versatile apparatus for brittle rock deformation. *International Journal of Rock Mechanics and Mining Sciences*, *66*, 114–123. https://doi.org/10.1016/j.ijrmms.2013.12.005

Collettini, C., Niemeijer, A., Viti, C., Smith, S. A. F., & Marone, C. (2011). Fault structure, frictional properties and mixed-mode fault slip behavior. *Earth and Planetary Science Letters*, *311*(3–4), 316–327. https://doi.org/10.1016/j.epsl.2011.09.020

Collettini, C., Tesei, T., Scuderi, M. M., Carpenter, B. M., & Viti, C. (2019). Beyond Byerlee friction, weak faults and implications for slip behavior. *Earth and Planetary Science Letters*, *519*, 245–263. https://doi.org/10.1016/j.epsl.2019.05.011

Crescentini, L. (1999). Constraints on slow earthquake dynamics from a swarm in Central Italy. *Science*, *286*(5447), 2132–2134. https://doi.org/10.1126/science.286.5447.2132

De Paola, N., Collettini, C., Faulkner, D. R., & Trippetta, F. (2008). Fault zone architecture and deformation processes within evaporitic rocks in the upper crust. *Tectonics*, *27*, T4017. https://doi.org/10.1029/2007TC002230

Dieterich, J. H. (1972). Time-dependent friction in rocks. *Journal of Geophysical Research*, *77*(20), 3690–3697. https://doi.org/10.1029/JB077i020p03690

Dieterich, J. H. (1979). Modeling of rock friction 1. Experimental results and constitutive equations. *Journal of Geophysical Research*, *84*(B5), 2161–2168. https://doi.org/10.1029/JB084iB05p02161

Fagereng, Å., Hillary, G. W. B., & Diener, J. F. A. (2014). Brittle-viscous deformation, slow slip, and tremor. *Geophysical Research Letters*, *41*, 4159–4167. https://doi.org/10.1002/2014GL060433.1

Fagereng, A., & Sibson, R. H. (2010). Melange rheology and seismic style. *Geology*, *38*(8), 751–754. https://doi.org/10.1130/G30868.1

Fang, Z., Dieterich, J. H., & Xu, G. (2010). Effect of initial conditions and loading path on earthquake nucleation. *Journal of Geophysical Research*, *115*, B06313. https://doi.org/10.1029/2009JB006558

Frank, W. B., & Brodsky, E. E. (2019). Daily measurement of slow slip from low-frequency earthquakes is consistent with ordinary earthquake scaling. *Science Advances*, *5*(10), eaaw9386. https://doi.org/10.1126/sciadv.aaw9386

French, M. E., & Zhu, W. (2017). Slow fault propagation in serpentinite under conditions of high pore fluid pressure. *Earth and Planetary Science Letters*, *473*, 131–140. https://doi.org/10.1016/j.epsl.2017.06.009

Gomberg, J., Wech, A., Creager, K., Obara, K., & Agnew, D. (2016). Reconsidering earthquake scaling. *Geophysical Research Letters*, *43*, 6243–6251. https://doi.org/10.1002/grl.54609

Gu, J., Rice, J., Ruina, A., & Tse, S. (1984). Slip motion and stability of a single degree of freedom elastic system with rate and state dependent friction. *Journal of the Mechanics and Physics of Solids*, *32*(3), 167–196. Retrieved from. http://www.sciencedirect.com/science/article/pii/0022509684900073, https://doi.org/10.1016/0022-5096(84)90007-3

Gualandi, A., Nichele, C., Serpelloni, E., Chiaraluce, L., Anderlini, L., Latorre, D., et al. (2017). Aseismic deformation associated with an earthquake swarm in the northern Apennines (Italy). *Geophysical Research Letters*, *44*, 7706–7714. https://doi.org/10.1002/2017GL073687

Hawthorne, J. C., & Bartlow, N. M. (2018). Observing and modeling the spectrum of a slow slip event. *Journal of Geophysical Research: Solid Earth*, *123*, 4243–4265. https://doi.org/10.1029/2017JB015124

Hawthorne, J. C., & Rubin, A. M. (2013). Tidal modulation and back-propagating fronts in slow slip events simulated with a velocity-weakening to velocity-strengthening friction law. *Journal of Geophysical Research: Solid Earth*, *118*, 1216–1239. https://doi.org/10.1002/jgrb.50107

Ide, S., Beroza, G. C., Shelly, D. R., & Uchide, T. (2007). A scaling law for slow earthquakes. *Nature*, *447*(7140), 76–79. https://doi.org/10.1038/nature05780

Ikari, M., Marone, C., Saffer, D. M., & Kopf, A. J. (2013). Slip weakening as a mechanism for slow earthquakes. *Nature Geoscience*, *6*(6), 468–472. https://doi.org/10.1038/ngeo1818

Ikari, M. J., Carpenter, B. M., & Marone, C. (2016). A microphysical interpretation of rate- and state-dependent friction for fault gouge. *Geochemistry, Geophysics, Geosystems*, *17*, 1660–1677. https://doi.org/10.1002/2016GC006286

Im, K., Elsworth, D., Marone, C., & Leeman, J. (2017). The impact of frictional healing on stick–slip recurrence interval and stress drop: Implications for earthquake scaling. *Journal of Geophysical Research: Solid Earth*, *122*, 10,102–10,117. https://doi.org/10.1002/2017JB014476

Ito, Y., Ikari, M. J., Ujiie, K., & Kopf, A. (2017). Coseismic slip propagation on the Tohoku plate boundary fault facilitated by slip-dependent weakening during slow fault slip. *Geophysical Research Letters*, *44*, 8749–8756. https://doi.org/10.1002/2017GL074307

Karner, S. L., & Marone, C. (2001). Frictional restrengthening in simulated fault gouge: Effect of shear load perturbations Stephen. *Journal of Geophysical Research*, *106*, 19,319–19,337.

Kato, A., Obara, K., Igarashi, T., Tsuruoka, H., Nakagawa, S., & Hirata, N. (2012). Propagation of slow slip leading up to the 2011 Mw 9.0 Tohoku-Oki earthquake. *Science*, *335*(6069), 705–708. https://doi.org/10.1126/science.1215141

Latorre, D., Mirabella, F., Chiaraluce, L., Trippetta, F., & Lomax, A. (2016). Assessment of earthquake locations in 3-D deterministic velocity models: A case study from the Altotiberina Near Fault Observatory (Italy). *Journal Geophysical Research: Solid Earth*, *121*, 8113–8135. https://doi.org/10.1002/2016JB013170

Leeman, J. R., Marone, C., & Saffer, D. M. (2018). Frictional mechanics of slow earthquakes. *Journal of Geophysical Research: Solid Earth*, *123*, 7931–7949. https://doi.org/10.1029/2018JB015768

Leeman, J. R., Saffer, D. M., Scuderi, M. M., & Marone, C. (2016). Laboratory observations of slow earthquakes and the spectrum of tectonic fault slip modes. *Nature Communications*, *7*, 11104. https://doi.org/10.1038/ncomms11104

Liu, Y. (2013). Numerical simulations on megathrust rupture stabilized under strong dilatancy strengthening in slow slip region. *Geophysical Research Letters*, *40*, 1311–1316. https://doi.org/10.1002/grl.50298

Mandl, G., de Jong, L. N. J., & Maltha, A. (1977). Shear zones in granular material—An experimental study of their structure and mechanical genesis. *Rock Mechanics Felsmechanik Mécanique Des Roches*, *9*(2–3), 95–144. https://doi.org/10.1007/BF01237876

Marone, C., Raleigh, B., & Scholz, C. H. (1990). Frictional behavior and constitutive modeling of simulated fault gouge. *Journal of Geophysical Research*, *95*(B5), 7007–7025. https://doi.org/10.1029/JB095iB05p07007

Marone, C., & Saffer, D. M. (2015). The mechanics of frictional healing and slip instability during the seismic cycle. *Treatise on geophysics*. Elsevier BV. https://doi.org/10.1016/B978-0-444-53802-4.00092-0

Marone, C. (1998). Laboratory-derived friction laws and their application to seismic faulting. *Annual Review of Earth and Planetary Sciences*, *26*(1), 643–696. https://doi.org/10.1146/annurev.earth.26.1.643

McLaskey, G. C. (2019). Earthquake initiation from laboratory observations and implications for foreshocks. *Journal of Geophysical Research: Solid Earth*, *124*, 12,882–12,904. https://doi.org/10.1029/2019JB018363

Mclaskey, G. C., & Yamashita, F. (2017). Slow and fast ruptures on a laboratory fault controlled by loading characteristics. *Journal of Geophysical Research: Solid Earth*, *122*, 3719–3738. https://doi.org/10.1002/2016JB013681

Miller, S. A., Collettini, C., Chiaraluce, L., Cocco, M., Barchi, M., & Kaus, B. J. P. (2004). Aftershocks driven by a high-pressure CO_2 source at depth. *Nature*, *427*(6976), 724–727. https://doi.org/10.1038/nature02251

Mirabella, F., Barchi, M., Lupattelli, A., Stucchi, E., & Ciaccio, M. G. (2008). Insights on the seismogenic layer thickness from the upper crust structure of the Umbria-Marche Apennines (central Italy). *Tectonics*, *27*, TC1010. https://doi.org/10.1029/2007TC002134

Nakatani, M. (2004). Frictional healing of quartz gouge under hydrothermal conditions: 2. Quantitative interpretation with a physical model. *Journal of Geophysical Research*, *109*, B07202. https://doi.org/10.1029/2003JB002938

Obara, K. (2002). Nonvolcanic deep tremor associated with subduction in southwest Japan. *Science*, *296*(5573), 1679–1681. https://doi.org/10.1126/science.1070378

Peng, Z., & Gomberg, J. (2010). An integrated perspective of the continuum between earthquakes and slow-slip phenomena. *Nature Geoscience*, *3*(9), 599–607. https://doi.org/10.1038/ngeo940

Porreca, M., Minelli, G., Ercoli, M., Brobia, A., Mancinelli, P., Cruciani, F., et al. (2018). Seismic reflection profiles and subsurface geology of the area interested by the 2016–2017 earthquake sequence (Central Italy). *Tectonics*, *37*, 1116–1137. https://doi.org/10.1002/2017TC004915

Reinen, L., & Weeks, J. D. (1993). Determination of rock friction constitutive parameters using an iterative least squares inversion method. *Journal of Geophysical Research*, *98*, 15,937–15,995. Retrieved from. http://www.agu.org/pubs/crossref/1993/93JB00780.shtml, https://doi.org/10.1029/93JB00780

Rice, J. R. (1983). Constitutive relations for fault slip and earthquake instabilities. *PAGEOPH*, *121*(3), 443–475. https://doi.org/10.1007/BF02590151

Rice, J. R., & Ruina, A. (1983). Stability of steady frictional slipping. *Journal of Applied Mechanics*, *50*, 343–349. Retrieved from. http://esag.harvard.edu/rice/105_RiceRuina_StabFrictSlip_JAM83.pdf, https://doi.org/10.1115/1.3167042

Rogers, G., & Dragert, H. (2003). Episodic tremor and slip on the Cascadia subduction zone: The chatter of silent slip. *Science (New York, N. Y.)*, *300*(June), 1942–1943. https://doi.org/10.1126/science.1084783

Romanet, P., Bhat, H. S., Jolivet, R., & Madariaga, R. (2018). Fast and slow slip events emerge due to fault geometrical complexity. *Geophysical Research Letters*, *45*, 4809–4819. https://doi.org/10.1029/2018GL077579

Rubin, A. M. (2011). Designer friction laws for bimodal slow slip propagation speeds. *Geochemistry, Geophysics, Geosystems*, *12*, Q04007. https://doi.org/10.1029/2010GC003386

Ruina, A. (1983). Slip instability and state variable friction laws. *Journal of Geophysical Research*, *88*(B12), 10,359–10,370. https://doi.org/10.1029/JB088iB12p10359

Ruiz, S., Metois, M., Fuenzalida, A., Ruiz, J., Leyton, F., Grandin, R., et al. (2014). Intense foreshocks and a slow slip preceded the 2014 Iquique Mw 8.1 earthquake. *Science*, *345*(6201), 1165–1169. https://doi.org/10.1126/science.1256074

Saffer, D. M., & Marone, C. (2003). Comparison of smectite- and illite-rich gouge frictional properties: Application to the updip limit of the seismogenic zone along subduction megathrusts. *Earth and Planetary Science Letters*, *215*(1–2), 219–235. https://doi.org/10.1016/S0012-821X(03)00424-2

Scholz, C. (1998). Earthquakes and friction laws. *Nature*, *391*, 37–42. Retrieved from. http://www.nature.com/nature/journal/v391/n6662/abs/391037a0.html, https://doi.org/10.1038/34097

Schubnel, A., Walker, E., Thompson, B. D., Fortin, J., Guéguen, Y., & Young, R. P. (2006). Transient creep, aseismic damage and slow failure in Carrara marble deformed across the brittle-ductile transition. *Geophysical Research Letters*, *33*, L17301. https://doi.org/10.1029/2006GL026619

Scuderi, M. M., Collettini, C., Viti, C., Tinti, E., & Marone, C. (2017). Evolution of shear fabric in granular fault gouge from stable sliding to stick slip and implications for fault slip mode. *Geology*, G39033.1. https://doi.org/10.1130/G39033.1

Scuderi, M. M., Marone, C., Tinti, E., Di Stefano, G., & Collettini, C. (2016). Precursory changes in seismic velocity for the spectrum of earthquake failure modes. *Nature Geoscience*, *9*, 695–700. https://doi.org/10.1038/NGEO2775

Segall, P., Rubin, A. M., Bradley, A. M., & Rice, J. R. (2010). Dilatant strengthening as a mechanism for slow slip events. *Journal of Geophysical Research*, *115*, B12305. https://doi.org/10.1029/2010JB007449

Shreedharan, S., Bolton, D. C., Rivière, J., & Marone, C. (2020). Preseismic fault creep and elastic wave amplitude precursors scale with lab earthquake magnitude for the continuum of tectonic failure modes. *Geophysical Research Letters*, *47*, e2020GL086986. https://doi.org/10.1029/2020GL086986

Shreedharan, S., Rivière, J., Bhattacharya, P., & Marone, C. (2019). Frictional state evolution during normal stress perturbations probed with ultrasonic waves. *Journal of Geophysical Research: Solid Earth*, *124*, 5469–5491. https://doi.org/10.1029/2018JB016885

Skarbek, R. M., Rempel, A. W., & Schmidt, D. A. (2012). Geologic heterogeneity can produce aseismic slip transients. *Geophysical Research Letters*, *39*, L21306. https://doi.org/10.1029/2012GL053762

Tinti, E., Fukuyama, E., Piatanesi, A., & Cocco, M. (2005). A kinematic source-time function compatible with earthquake dynamics. *Bulletin of the Seismological Society of America*, *95*(4), 1211–1223. https://doi.org/10.1785/0120040177

Tinti, E., Scuderi, M. M., Scognamiglio, L., Di Stefano, G., Marone, C., & Collettini, C. (2016). On the evolution of elastic properties during laboratory stick-slip experiments spanning the transition from slow slip to dynamic rupture. *Journal of Geophysical Research: Solid Earth*, *121*, 8569–8594. https://doi.org/10.1002/2016JB013545

Trippetta, F., Collettini, C., Meredith, P. G., & Vinciguerra, S. (2013). Evolution of the elastic moduli of seismogenic Triassic evaporites subjected to cyclic stressing. *Tectonophysics*, *592*(2013), 67–79. https://doi.org/10.1016/j.tecto.2013.02.011

Ujiie, K., Saishu, H., Fagereng, Å., Nishiyama, N., Otsubo, M., Masuyama, H., & Kagi, H. (2018). An explanation of episodic tremor and slow slip constrained by crack-seal veins and viscous shear in subduction mélange. *Geophysical Research Letters*, *45*, 5371–5379. https://doi.org/10.1029/2018GL078374

Viesca, R. C., & Garagash, D. I. (2015). Ubiquitous weakening of faults due to thermal pressurization. *Nature Geoscience*, *8*(11), 875–879. https://doi.org/10.1038/ngeo2554

Wallace, L. M., Webb, S. C., Ito, Y., Mochizuki, K., Hino, R., Henrys, S., et al. (2016). Slow slip near the trench at the Hikurangi subduction zone, New Zealand. *Science*, *352*(6286), 701–704. https://doi.org/10.1126/science.aaf2349

Wech, A. G., Creager, K. C., Houston, H., & Vidale, J. E. (2010). An earthquake-like magnitude-frequency distribution of slow slip in northern Cascadia. *Geophysical Research Letters*, *37*, L22310. https://doi.org/10.1029/2010GL044881